PREDICTION OF THE CUTTING FORCES FOR ROBOTIC GRINDING PROCESSES WITH ABRASIVE MOUNTED BITS

A THESIS SUBMITTED TO
THE GRADUATE SCHOOL OF NATURAL AND APPLIED SCIENCES
OF
MIDDLE EAST TECHNICAL UNIVERSITY

BY

KEMAL AÇIKGÖZ

IN PARTIAL FULFILLMENT OF THE REQUIREMENTS
FOR
THE DEGREE OF MASTER OF SCIENCE
IN
MECHANICAL ENGINEERING

SEPTEMBER 2015

Approval of the thesis:

PREDICTION OF THE CUTTING FORCES FOR ROBOTIC GRINDING PROCESSES WITH ABRASIVE MOUNTED BITS

submitted by **KEMAL AÇIKGÖZ** in partial fulfillment of the requirements for the degree of **Master of Science in Mechanical Engineering Department, Middle East Technical University** by,

Prof. Dr. Gülbin Dural Ünver
Dean, Graduate School of **Natural and Applied Sciences** _____

Prof. Dr. R. Tuna Balkan
Head of Department, **Mechanical Engineering** _____

Assoc. Prof. Dr. E. İlhan Konukseven
Supervisor, **Mechanical Engineering Dept., METU** _____

Examining Committee Members:

Prof. Dr. R. Tuna Balkan
Mechanical Engineering Dept., METU _____

Assoc. Prof. Dr. E. İlhan Konukseven
Mechanical Engineering Dept., METU _____

Asst. Prof. Dr. A. Buğra Koku
Mechanical Engineering Dept., METU _____

Asst. Dr. M. A. Hüsnü Dal
Mechanical Engineering Dept., METU _____

Assoc. Prof. Dr. Ali Oral
Mechanical Engineering Dept., Balikesir University _____

Date: 11.09.2015

all information in this document has been obtained and presented in accordance with academic rules and ethical conduct. I also declare that, as required by these rules and conduct, I have fully cited and referenced all material and results that are not original to this work.

Name, Last Name: Kemal AÇIKGÖZ

Signature:

ABSTRACT

PREDICTION OF THE CUTTING FORCES FOR ROBOTIC GRINDING PROCESSES WITH ABRASIVE MOUNTED BITS

Açıkgöz, Kemal

M. S., Department of Mechanical Engineering

Supervisor: Assoc. Prof. Dr. E. İlhan Konukseven

September 2015, 87 pages

In this study, cutting forces for robotic grinding processes with mounted bits are investigated. In the majority of the grinding literature, the grinding process is analyzed based on rigid grinding machines and larger size wheels. However, the robotic grinding systems involve small size tools. Therefore, currently there is a need to experimentally study the geometry and force relationships for mounted bits. In order to overcome some of the difficulties arising in grinding studies (e.g. need for dressing, cooling, etc.), cBN (cubic Boron Nitride) tools are utilized. Tangential and Normal forces for a given geometry during the operation are predicted as the outcome for use in robotic grinding operations. This predicting model is developed in a controlled environment -an experimental setup- which is specifically designed for measuring required system parameters for the model.

Keywords: Robotic Grinding Process, Force prediction for Grinding, Parallel Manipulators in Grinding Operation.

ÖZ

AŞINDIRICI TAŞ KULLANILAN ROBOTİK TAŞLAMA PROSESLERİNDE KESME KUVVETLERİNİN TAHMİNİ

Açıkgöz, Kemal

Yüksek Lisans, Makine Mühendisliği Bölümü

Tez Yöneticisi: Doç. Dr. E. İlhan Konukseven

Eylül 2015, 87 sayfa

Bu çalışmada, aşındırıcı taş kullanılan robotik taşlama süreçleri için kesme kuvvetleri araştırılmıştır. Taşlama literatürünün çoğunluğunda, taşlama prosesi, rijit makineler ve büyük çaplı taşlar kullanılarak analiz edilmiştir. Ancak, robotik taşlama sistemlerinde küçük taşlar kullanılmaktadır. Bu sebeple, günümüzde aşındırıcı taşlar için geometri ve kuvvet ilişkilerinin deneysel olarak çalışılmasına ihtiyaç duyulmaktadır. Bu çalışmada, taşlama sistemlerinde karşılaşılan bazı zorluklarla karşılaşmamak için (örneğin giydirme ihtiyacı, ya da soğutma ihtiyacı) cBN (kübik bor nitrür) taşlar kullanılmıştır. Taşlama esnasında teğetsel ve dik kuvvetlerin verilen bir geometri için tahmini, robotik taşlama operasyonlarında kullanılmak üzere sonuç olarak elde edilmiştir. Bu model, gerekli sistem parametrelerinin ölçülebilmesi için özellikle tasarlanmış kontrollü bir çalışma ortamında (deney düzeneğinde) elde edilmiştir.

Anahtar Kelimeler: Robotik taşlama prosesi, Taşlama için kuvvet tahmini,Taşlama operasyonlarında paralel manipülatörler.

ACKNOWLEDGEMENTS

I want to express my deepest gratitude to my thesis supervisor Assoc. Prof. Dr. E. Ilhan KONUKSEVEN for his guidance, advice, criticism, encouragements and insight throughout this research.

During the course of this work, the presence and friendship of the TUBITAK project group (114E274) has been most pleasurable. I want to thank to M. Sc. student Uğur MENGİLLİ, Res. Asst. Abülhamit DÖNDER, Ph. D. student Masoud LATIFI-NAVID, M. Sc. student Mahmoud Nemer, and Ph. D. student Mahmood LAHROODI for their comments and constructive criticism throughout the thesis.

I also want to mention the support of M. Sc. student Payam PARVIZI on the manufacturing of one of the test setup parts.

This thesis is funded by TUBITAK, project grant no: 114E274.

To my parents,

with the deepest gratitude

TABLE OF CONTENTS

LIST OF FIGURES

FIGURES

LIST OF TABLES

TABLES

LIST OF SYMBOLS

cBN	Cubic Boron Nitride type superabrasive wheel
F/T	Force/Torque
ANN	Artificial Neural Network
ADOC	Actual Depth of Cut
SDOC	Set Depth of Cut
μ	Friction coefficient
K	Grinding stiffness

CHAPTER 1

INTRODUCTION

1.1.Robotic Grinding Systems

Robotic grinding is a robotic finishing method. The workpieces machined via different manufacturing methods, possess form errors or burrs on their surfaces. These parts must be ground and burrs must be removed before the delivery of the parts. This operation is important for automotive and aerospace industries where, for the deburring case, involves dexterity requiring and health threatening manual operations (an example for manual deburring can be seen in **Figure 1**).

Figure 1 - A worker while deburring a jet engine part [1]

The development of super-abrasives (diamond, and cubic boron nitride - cBN) along with the advance of path planning algorithms utilizing force/impedance control techniques have led to the development of quality defining robotic grinding systems. These systems use simple cutting models for abrasive tools. These models, generally, do not include effects of spindle speed, depth of cut, and feed rate (or work-piece speed) but consider the problem as a control problem (exceptions are robotic belt

grinding, and robotic polishing). The motivation of this thesis is to open up a way to use these additional control parameters by analyzing their effects on the forces for the robotic grinding operations.

In order to understand the purpose of this thesis better, the computer controlled (CNC) grinding machines must be considered separately from the robotic grinding systems. For these machines, the cutting force models are utilized in order to compensate the depth of cut and wheel speed for the desired surface quality or for finishing the operation in high speed. Playing with these parameters is not easy for robotic grinding operations, because of the fact that a robotic grinding system has lower stiffness than these machines typically have [2]. Therefore, stiffness of the machine is an important factor. Thus, under the influence of low stiffness of the system, the motivation behind the analysis of the effect of system parameters (i.e., depth of cut, spindle speed, and feed-rate) on the forces is sound and the results can be very useful in industry. Therefore the main points can be expected by the reader on this fine detail throughout the thesis.

Serial manipulators with a deburring or grinding tool are commonly used in industry. Typically in these systems there is also a multi-axis F/T (i.e. force/torque) sensor. Force control, or impedance control are the typical control methods in these systems, and details of these methods can be found in [3]. This work does not include the control aspects of the operation. However, if the reading process is accompanied by the particular literature, readers can achieve a better understanding. In this thesis, the author diverges from utilization of a standard serial manipulator. In order to study the system parameters' effect on the forces; an experimental setup is built using a parallel manipulator, a high speed spindle and a multi-axis force/torque sensor. A novel idea, mentioned first by [4], involves a hybrid serial - parallel robot to use in robotic deburring. The usage of a parallel manipulator can be justified by its high precision (high precision, but limited workspace); whereas the usage of a serial manipulator can be justified by its high reachability (high workspace volume, but low precision). Thus, combination of these two configurations offer both high reachability and high precision. Targeting the same application novelty, the thesis focuses on a parallel

manipulator's capability for robotic grinding, which is among the motivating forces of this work. Hence, a hybrid serial – parallel manipulator can be developed basing this study. Construction details for the parallel manipulator part are given in this thesis in Chapter 3 and can be easily extended to a hybrid serial – parallel robotic system by mounting the parallel manipulator part to a serial manipulator as an end-effector.

1.2.Grinding Process Forces

As happens for any metal cutting operations, the cutting forces are of prime importance in grinding as well. These forces are the main indicators of the process efficiency (heat is equally important, but not covered in this thesis). The cutting tools, such as grinding wheels, have important factors that affect the process efficiency. The forces are highly related to the cutting tool of use. Therefore, the tool (chosen with respect to the material of the workpiece), spindle speed, depth of cut, and feed-rate are pivotal system parameters in grinding that affect the forces.

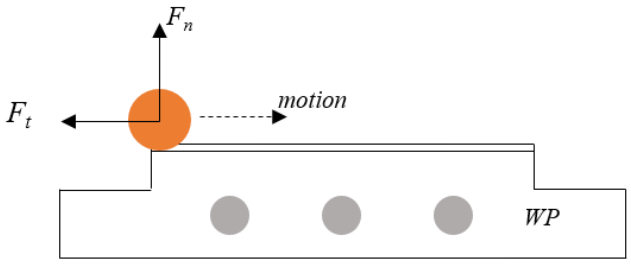

Figure 2 - The top view of the workpiece (WP), tool and the normal and tangential forces.

As a typical robotic grinding operation, for simplicity, **Figure 2** can be considered. The tool is shown by the orange circle. During the operation, the workpiece is fixed (this is one of the differences in robotic grinding, where for a CNC grinding operation, generally the workpiece moves but the wheel is fixed). The wheel (or the tool) is given a penetration (depth of cut) in normal direction, where it moves along the tangential direction. Therefore, in this example, a layer of material is removed.The

cutting forces in grinding operations are mainly the tangential ($\vec{F}_t$) and normal ($\vec{F}_n$) forces (shown in **Figure 2**). The radial force in the direction along $\vec{F}_t \times \vec{F}_n$ is generally ignored because of its experimentally observed uncorrelated behavior and zero mean value.

The forces changes with different geometry of interaction, tool shape (cylindrical, spherical, etc.), and angle of tool. Thus, a simplified geometry can help model development (mapping). The tool workpiece interaction, as in **Figure 2**, results in different values of tangential and normal forces. Moreover these forces, are highly related with the tool's direction of rotation (clockwise or counter clockwise) and the grinding modes corresponding to rotation of the tool and motion of the tool are called "up grinding" or "down grinding" [5].

1.3.Motivation

The motivation for this thesis does not only not only come from the aim to predict the forces during grinding operations involving robots. It is also nourished from the will to predict them in favor of increasing the number of controllable system parameters to use in interaction control (force/impedance control) scenarios. In force/impedance control, the main control parameter is the motion (depth of cut, and speed of the end-effector). However, when an abrasive tool is used, the control parameters can be spindle speed, and motion (depth of cut, and feed-rate). Therefore, the controller can use the spindle speed as an additional control parameter, thus achieve the control action. In robotic grinding literature, there are several examples [6], [7] in which the motion and force were related via simple proportionality constant, namely the stiffness, K. However, as obtained in this thesis, the relationship is nonlinear. Thus, a mapping from spindle speed, depth of cut, and feed-rate to normal and tangential forces is important and sought.

An important aspect of this thesis study is its future application on grinding turbine airfoil components, additionally it will also be used for deburring of these parts. The requirement of low fatigue and stress in these operations, imposes usage of creep feed grinding approach. In creep feed grinding, typically the grinding wheel is given a full

depth of cut, and requires only a few passes to remove full stock. In conventional traverse surface grinding, even thousands of passes may be required. Due to this difference, the creep feed grinding has advantages including increased accuracy, efficiency, surface finish quality and burr reduction. However, since creep feed grinding is accompanied by high forces, a creep feed grinding machine must be rigid and powerful. The grinding forces could cause bending of the wheel root in robotic grinding operations, and the machining accuracy will be lost (can be corrected if the forces are predicted). The robotic application of creep feed grinding (low stiffness due to a serial manipulator) may be difficult from this perspective, but the application is an industrial requirement. Mechanism of material removal, wheel wear, temperature distribution, efficiency, and productivity of the grinding process are affected by grinding forces; thus the grinding force is one of the main factors determining the machining quality [8].

Figure 3 - CBN Internal grinding tools [9]

cBN abrasive mounted bits, as shown in the **Figure 3**, are used in precision robotic grinding operations because of their excellent wear resistance, and heat dissipation properties, despite their high costs [10].These tools are in superabrasives category. In this work, cBN wheels are utilized only for their usefulness in avoiding unnecessary complications [11] (such as frequently dressing due to wear, or need for coolants). Therefore, with a cBN wheel, a dry (without coolant) and continuous operation is possible. Moreover, the author expects more and more examples on interaction

control using cBN (or other super-abrasives) wheels in robotic deburring operations for the incoming years. Currently, the carbide rotary files are the common tools in robotic deburring operations.

The physics of the problem defined in this thesis involves a non-standard grinding machine developed during the thesis. A parallel manipulator and a cBN internal grinding wheel are combined as another aspect of this study. By using the information (experimental setup design, and construction directives) gathered in this study, a serial – parallel hybrid robotic deburring or grinding system can be built. The idea of mounting the experimental setup's relevant structures to a serial manipulator's end effector can offer both high precision and reachability [4], **Figure 4**. Unlike [4], a commercial parallel manipulator is used in this study.

Figure 4 - Serial and parallel combination to use in force/impedance control scenarios [4]

The experimental setup is designed to be able to study many of the grinding process aspects not only for the purpose of the present thesis but also for future academic research. The custom built experimental setup has several capabilities, thus versatility is sought. The setup has a manual tool changer, from which different end-effectors can be mounted. One of the end-effectors is a laser-displacement sensor and can be

used for surface scanning (in order to study the surface quality after the operation). The base of the experimental setup also has a high speed single axis piezo-electric actuator. This actuator can be used for interaction control studies (parallel manipulator is very slow compared to this actuator, See Appendix A.1 and Appendix A.2). The linear stages are from Parker Company.

1.4.Thesis Layout

The thesis work is spread out to six major chapters.

Following the introduction part being Chapter 1, Chapter 2 as the literature survey part, includes the presentation of similar studies and current state of the art are together with the discussion on the experimental setup and its place in literature. Additionally, the grinding process mapping methods, regarding force prediction is discussed. This chapter also focuses on The Neural Network based methods, and relevant methods from the literature. Also the grinding process monitoring for grinding burn and chatter detection is discussed.

In Chapter 3 the experimental setup is presented. The setup design, the device properties and construction details are given. This section holds the basis for building a hybrid serial – parallel deburring system (focused only to the end-effector part, which is the most important part when it comes to design of such a system). The communication libraries for the devices are discussed. The software that control the devices and records the forces is explained.

In main chapter of this thesis, Chapter 4, the cutting force prediction using "Neural Networks" is discussed. The experiments are discussed also in this section. The initial surface preparation to make the cBN tool parallel to the workpiece surface is explained. The experiments are considerably different than what has been done in literature. The process chart, and how it is obtained are presented, related with the high importance of process charts in grinding process [12]. Finally, a verification (verifying the mapping quality of the Neural Network) table is given. This table shows the accuracy of the model for untaught patterns presented to the network.

In Chapter 5, the kinematic calculations of the offset imposed by mounting the spindle is mathematically obtained. This offset error is important (since it introduces angles that makes the prediction of cutting forces difficult). According to the analysis, a 2 degree rotation is given to the spindle in +Z direction of the parallel manipulator (in order to make it perpendicular to the workpiece).

Chapter 6 includes, the conclusions drawn upon the overall study. Additionally, the ways to improve the prediction results (Chapter 4) are also given. Further implications and potentials of this work is also discussed in this chapter.

CHAPTER 2

LITERATURE SURVEY

2.1. The Grinding Process Modeling: State of the Art

In this section, the grinding process modeling (for simulation) and the state of the art is presented. Since, the grinding process is an extremely broad field of study, it requires some restrictions on the literature review. Before listing the restrictions, the broadest sense of modeling for grinding operations is given (what can be the inputs for a grinding process model, and what are the outputs?). The grinding process modeling is not limited to the prediction of forces but can involve prediction of the surface quality or time to remove material, or even feasibility of using a specific tool (for instance, a model may predict whether or not a diamond abrasive can be used for grinding high carbon steel parts). A full review of the different aspects of modeling of the grinding process can be found in [13].

As defined, from manufacturing point of view, by Tönshoff et al. [14]; a model is an abstract representation of a process which maps (to pull off technologically relevant predictions) inputs (causes) to the outputs (effects). Within this context, the model is not developed for the broadest sense, that is, it does not map all the causes to the effects, but it is restricted to what is technologically relevant for an application or case. For instance, a model for a wheel made of Al_2O_3 grits may not be suitable for a wheel made of cBN grits, since the geometry and the hardness of the grits are different. Moreover, a model developed for a specific grinding machine may not be suitable for another grinding machine.

The models in grinding process can be subdivided into physical and empirical models [14]. Physical models uses basic physical laws and involves obtaining mathematical relationships between inputs and outputs. On the other hand, empirical models requires experimental knowledge. In empirical models, grinding process outputs are

related to inputs by model constants. These constants are determined from experiments. Monitoring of causes and effects is required. The main idea behind physical models is that the resulting model (based on basic physical laws which are universal and does not care the application) can be generalized easily to other grinding operations and conditions [13].There is a compromise between model accuracy and the time and effort required to obtain the model. The experimental studies may take time and real effort, but accuracy can be very high. The experiments are performed for specific grinding conditions and grinding machines or processes. The empirical models are bound to that conditions or the machines and generally it is not possible to use an empirical model under different conditions, or for different grinding machines and grinding processes. In physical modeling, the model development may be mathematically involved and require a broad understanding of the underlying physics, but the results are generally applicable to different grinding conditions or machines. Both empirical models and physical models are suitable for model based control systems design. However, since the empirical models are targeted to the application where the controller will be designed, the accuracy of the model can help developing a better control system.

In [13], the grinding process models are subdivided into Molecular Dynamics (MD), Kinematics, Fundamental, Finite Element Analysis (FEA), Regression, Artificial Neural Networks (ANN), and Rule Based models.

In kinematics only approach, the contact geometry between the workpiece and the grains on the wheel is considered. Typically, grains are modeled as two dimensional shapes. Modeling of the surface profile after the grinding operation is the major concern of this approach [13].

Varieties of the kinematic approach includes kinematic-geometric modeling. The penetration of the grains are modeled in detail. By the three-dimensional and detailed individual grain/workpiece interaction, the volume removed by each grain can be calculated. This approach is directed towards microscopic cutting (micro-cutting) in grain level by considering each grain as microscopic cutting tools. Using the calculated volume, the specific grinding forces can also be calculated for each grain

and the summation of the forces within the wheel workpiece contact region gives the net force. The micro-cutting in kinematic-geometric approach can be taken as ideal (that is, the grains cut entire workpiece along their trajectory) but non-ideal deviations can also be added to the model. These deviations include material pile-up (ploughing) and rubbing (sliding without cutting). Each grain on the wheel, at any time during the operation is in one of the three modes of micro-cutting (rubbing, ploughing and cutting) [15]. Therefore, the net force is dependent on these modes and their contributions. The kinematic-geometric modeling requires computational power.

The detailed review of the ANN models are given in the following subsection.

2.2. ANN in Grinding Process Modeling

The ANN models are successfully applied to many practical scenarios [16] because of their several properties [17], [18]. ANN can model a system without knowing its underlying physics; only inputs and outputs are important. ANNs are global function estimators (universal approximation theorem [19], [20], [21], which is basically telling for any function, there must be a neural network structure that can mimic it), which is what makes them attractive. Moreover, ANNs can be combined with physical as well as kinematic-geometric models to improve the model quality. Beyond the limited literature required by the necessities of the present work there are excellent books on ANNs [22], [23], [17].

ANN models can be designed as both output estimators (surface roughness, grinding forces, residual stress, flexural strength, etc.) and input estimators (that is, model predicts the necessary inputs for a desired output). ANN can also be used for process monitoring (in order to predict the grinding burn and chatter, [24], [25]).

ANN models are trained based on the experimental data. The experimental data is generally given to the ANN by structured tables or lists of the inputs and outputs recorded during the operation. For ANNs in system identification, there are also online learning methods that constantly learns and maps the inputs and outputs for identification of the dynamic system of concern. For ANNs in system identification

please refer to [26]. The mapping of the inputs and outputs is static in the present study.

A typical static ANN training table (formed by the data gathered from experiments) for grinding process modeling can contain the following information [13]:

The model inputs: Material removal rate (MRR), workpiece speed, wheel speed, feed rate, etc.

Recorded quantities: Acoustic emissions, grinding forces, and grinding power, etc.

Model outputs: Surface roughness, grinding forces, residual stress, flexural strength, etc.

The mathematical derivation of the relationships is provided in the ANN modeling section (Section 4.4).

The model training set can be subdivided into two. The first part is used for training (usually 80%) and the second part is used for verification (usually 20%) to select the model complexity. Verification of the model is based on the experiments that are not known to the model during the training phase. The verification data is organized using the same structure obtained for the training data. "Additionally, cross-validation (CV) can also be used. The training data is split into K sections, for each section k $\in\{1,\ldots,K\}$, we train based on all the sections but the kth." [27].ANN models are mainly posed to generalization scenarios after the training phase. These scenarios involve model testing for un-taught inputs. The results of the generalization tests are good indicators of the model quality [27].

There is a particularly interesting examples from literature on utilization of ANNs for grinding process modeling. In the work [8], a creep feed grinding process is studied. The neural network back propagation (BP) algorithm, also given in Section 4.4, is improved by introducing error distribution function (EDF). Based on this technique, the forces during the creep feed grinding were predicted with 6% error and even 3% error values were reached. These error values are highly respectful because of the

complex nature of the grinding process. In this thesis work, we took a similar approach and found similar error values with BP only approach. However, the methods and the process is considerably different than the present study (differences are that the experimental setup is robotic in the present study, and the neural network is trained with MATLAB's neural network toolbox [28]).

2.3. Experimental Setup

In the robotic deburring and grinding literature force/torque sensors are commonly utilized. The sensor is mounted either before the end-effector on the robot, or under the workpiece on the machine base. Additional to this configuration, there are also cases where a linear variable differential transducer (LVDT) is used. In this configuration, instead of measuring the forces, the change of the length of the LVDT is used. However, this indirect force measurement is not accurate.

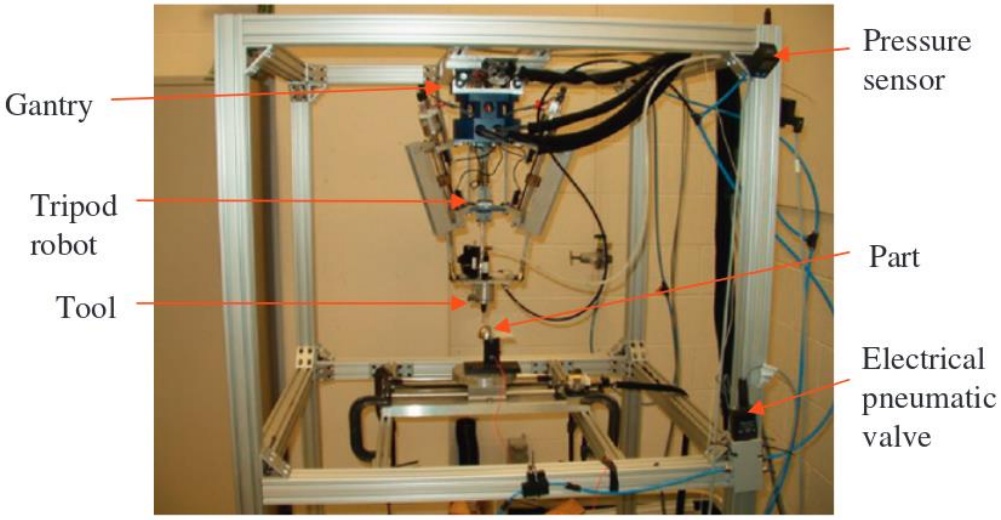

Figure 5 - Ryerson University pneumatic parallel deburring robot [29].

There are robotic deburring applications which uses abrasives and parallel mechanisms. In Figure 4 a parallel manipulator with pneumatic actuators can be seen [29]. In this system, instead of a force/torque sensor LVDT was used. The tool is Al_2O_3 .Additionally, the mechanics of the cutting was developed for the particular

deburring operation, which is similar to physical models (based on Hertzian contact theory) in grinding.

The study in [29] is similar to this thesis work as it tries to develop a deburring model for abrasive mounted bits. Moreover, the setup itself is also similar.

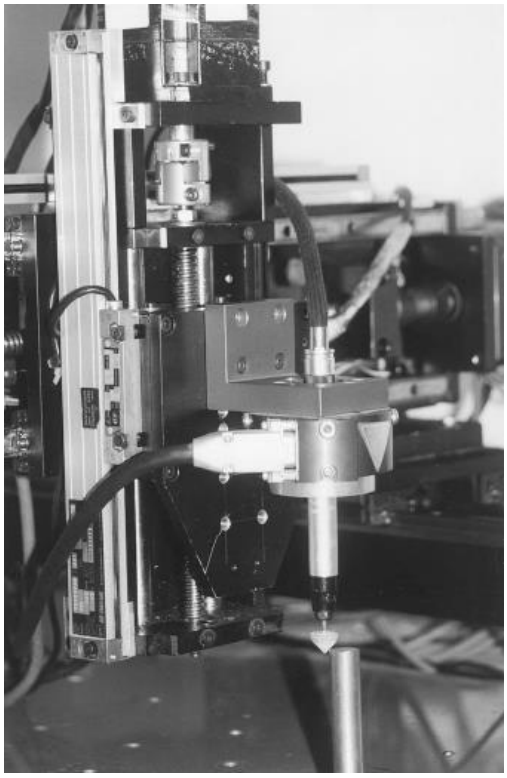

Figure 6 - Circular profile chamfering (deburring) robot [30].

In [30], a compliant mechanism is displayed. The mentioned difficult modeling of the process was bypassed by an online rule self-regulating fuzzy controller (RSFC). In this study, a Cartesian robot was used. The chamfering along a circular object was performed based on force control (force maintained at a desired level).The robotic deburring on unknown contours was achieved. A force sensor with resolution of 0.01 kgf was installed on the manipulator. The cutter was a grinding wheel which was mounted to a spindle (that rotates at 30000 RPM). A constant desired force between the tool and the workpiece was set and compensated. This application is a typical robotic deburring/grinding case where a grinding process model could be applied.

The force model was considered only for tangential case $F_t = K \times MRR$. The material removal rate was given as $MRR = \left(A_{chamfer} + A_{burr}\right) \times V_W$ (For detailed descriptions of the symbols and the process please refer to the original paper [30] or for the symbols see **Figure 7**). The spindle speed effect and the feed-rate as well as the amount of penetration was ignored in the controller.

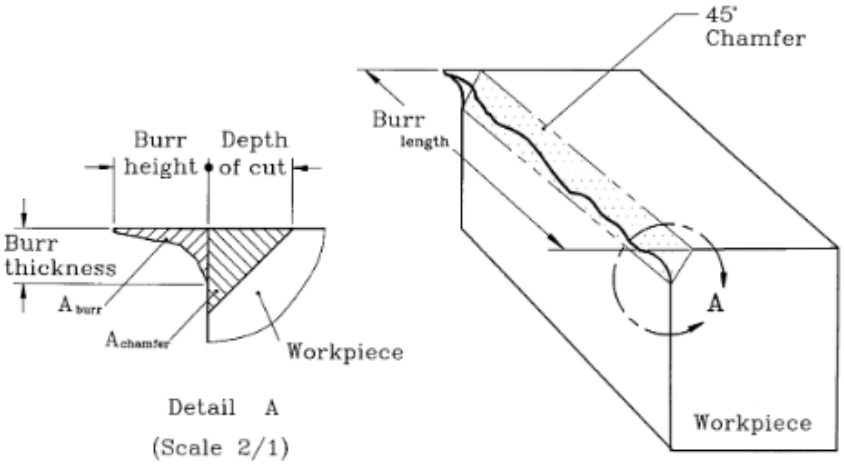

Figure 7 - Details of the burr shape and relevant symbols [30].

In addition to these examples, there are specially developed compliant tools for deburring. One example is shown in Figure 8.

Figure 8 - A compliant deburring tool from ATI Company

In this example, a compliant deburring tool with carbide rotary file can be seen. There is also a force/torque sensor on the end-effector. The compliancy is in radial and axial directions. The tool is pneumatically supplied and the compliancy can be adjusted via the pressure supplied within the tool. For different types of compliant deburring tools please refer to the company's website [31].These systems utilize passive compliance. However, there are active compliance examples, too. For instance, the previous example of parallel pneumatic system is an example of active compliance [29].

The experimental setup designed and built during the thesis studies takes advantage of cBN wheels, a commercial parallel manipulator, a force/torque sensor and high-speed spindle. The aforementioned examples are shared in this section to illustrate the extent of the present work.

2.4. Additional Review and Concepts

In [32],the grinding system was considered as a whole, including machine tool, fixture and workpiece. Effect of the dynamics of the system were analyzed. The model was dynamic and found using MRR by the following formula,

$$MRR = V_W a \tag{1}$$

The workpiece material is modeled and stored in the memory as Z-buffer values (height). Using geometric engagement calculations with a computer simulation, the following formulation was introduced, and the normal and tangential forces for each buffer element was calculated based on the Equation (3).

$$f_n^i = \frac{ECC.MRR^i}{V_S} \tag{2}$$

$$F_n = Kb\left(\frac{V_W}{V_S}a\right)^{\varepsilon} \tag{3}$$

$$F_t = \mu F_n \tag{4}$$

From the experimental study, the model parameters were found (K, ε, μ), using linear least squares solution. The experiments were done with a grinding machine with 30 N/μm stiffness. As the final result, the mean cutting forces were predicted with 25% error.

In order to deal with the difference in set depth of cut (SDOC) and actual depth of cut (ADOC); the machine stiffness, the workpiece tool contact stiffness, and cutting stiffness (grinding stiffness) must be considered. In [33], the SDOC and ADOC were analyzed. During the study, workpiece was fixed with a fixture which allowed changing the machine stiffness (5 μm – 40 μm). During the experiments, for a given stiffness value that is set by the fixture, SDOC, and operation conditions the ADOC was observed. This observation was done based on a multi-pass method. As an example, a 10 μm SDOC was given and the forces during the operation were recorded. Then starting from 6 μm the SDOC was increased by 0.5 μm in each pass until a force was observed.

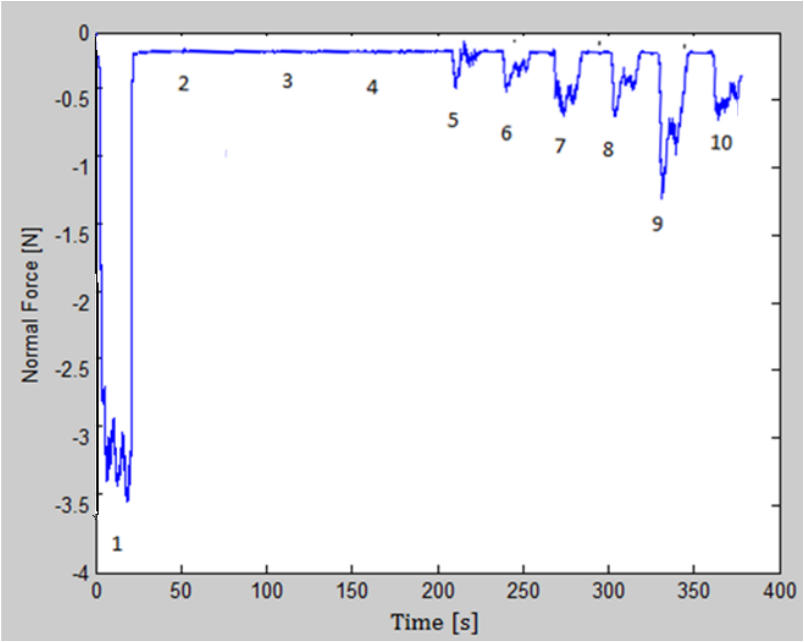

Figure 9 - Multi-pass experiment. The numbers indicates the pass number.

The same procedure in [33] is utilized in this thesis and the force patterns shown in **Figure 9** are observed. In each pass a 10 μm increase is given. According to the study the ADOC for 200 μm SDOC, 15000 RPM and 0.2 mm/s feed is observed in 5th pass which corresponds to 130 μm. Note that the second pass is started from 100 μm. (There is a mean 0.2 N cable force during the operation). From this experiment, the stiffness factor, K is found as,

$$K = \frac{ADOC}{SDOC} = \frac{130}{200} = 0.65 \qquad (5)$$

The grinding process modeling in terms of dynamics of interaction and micro-modes (sliding, ploughing, and cutting) of grinding were investigated in [32]. The model in [32] was regarded as a time dependent process, therefore the process operation conditions were taken into consideration. The grinding wheel geometry as well as time dependent wheel condition were included. However, an experimental setup was needed for testing the developed model.

In one side of grinding process modeling (for instance, the model in [32]), the models are complicated and involves utilization of every aspect of the grinding process parameters (material properties, wheel properties, micro-cutting action, operation conditions, etc.). Whereas, on the robotic grinding side, the utilization of the grinding process models developed separately for CNC grinding machines are under-utilized and control systems are trusted more than the grinding process models.

For autonomous grinding, the main source of information is the force data coming from the interaction of the tool and the workpiece [34]. Similarly for robotic grinding process modeling (modeling the grinding operation to use in robotic grinding), the main information source is the force sensor. For different operation conditions, such as spindle speed and the feed-rate (assuming the spindle is connected to the robot end-effector, the feed-rate can be taken as the speed of the end-effector along the material removal direction), the force prediction can be useful (especially for the simulation). As an example, the reader can imagine an operator removing burrs using a hand-held deburring tool. The process model, in this case can deal with the wheel speed, workpiece material, and the speed of the hand of the operator. By using this

information, an application of haptic device simulating the deburring operation can be built. Based on this simulation requirements, the operator hand motions during deburring can be recorded and analyzed, thus the motion primitives can be obtained for deburring operation. Also, the haptic application can be used for training of operators. The motion primitives associated with the human deburring capabilities can be mapped to a robotic deburring system, hence utilizing the human operator brain modeling (experience) in interaction control case [3].

Force control concept can be illustrated with an analogy, suppose a person carrying a bucket with one hand. In the bucket there are heavy spherical objects which can move arbitrarily. In order to move the bucket along a straight line while standing still, the person must control the force applied to the bucket by controlling the joint forces in his/her arm. The force control tries to compensate and keep forces along a trajectory constant during material removal (such as in robotic grinding, deburring or polishing cases). In robotic deburring literature, the main trend is the interaction control (impedance control, see [3]). Rather than only trying to control the forces, in interaction control, the process (for instance the spindle speed in grinding can be controlled) by which the material removed is controlled.

On robotic grinding side, there are lots of studies focusing on belt grinding operation. In [6], a belt grinding robot in which the work-piece mounted on the end-effector case was considered. The robot moves the workpiece along a trajectory and makes the workpiece contact with the belt grinder. In order to obtain a smooth finish, a constant contact force between the workpiece and the grinder was controlled. However, more than the grinding process modeling, the force based calibration of the robot was focused. Only a linear relationship between the force and the displacement (along the material removal direction) was taken. Furthermore, a constant stiffness parameter k describing the contact stiffness of the system for the robotic belt grinding operation was utilized in the equations. Similar robotic belt grinding analyses are present in literature. As an example of complex modeling regarding the grinding process dynamics in robotic belt grinding, the reader can refer to [35]. The process considered was similar to [6] (robotic belt grinding). The study referred previous studies on

robotic belt grinding and utilized force sensors and energetic aspects of the grinding process. However, their grinding wheel (belt grinder) is completely different than the wheel used in this dissertation (cylindrical cBN internal grinding wheel with 4 mm diameter, 126 µm average grit size). Also in [35] high workpiece speeds (i.e., speeds more than 5 mm/s) were investigated. Despite many differences, the main theme is similar to the present study.

CHAPTER 3

EXPERIMENTAL SETUP

3.1. Introduction

In this thesis work, a grinding robot as an experimental setup is designed. In this setup, we utilized Hexapod, high frequency spindle, Force/Torque sensor, cBN abrasive bits, collets, tool changer, piezo actuator, and laser displacement sensor. These tools are combined so that we can perform grinding in a controlled environment. This approach allows us to study the mechanics of grinding (e.g., cutting efficiency, forces). In following sections, the test setup design and auxiliary software for the setup are discussed.

This setup is designed as the first step towards the realization of a hybrid serial – parallel deburring/grinding robot [4] based on a commercial parallel manipulator. In addition, the parallel manipulator's adaption to a typical grinding case is achieved. Including the cBN grits and a high-speed spindle, this experimental setup is tailor made for the study of the grinding process for robotic applications. However, for future research, the setup must be isolated from the environment by a cleanroom which prevents the heat variations.

3.2. Setup Overview

The purpose of the setup is to create a controlled environment for developing grinding process model and testing control algorithms for grinding process for further research. We utilized a tool changer (shown as number 3 in **Error! Reference source not found.**) that allows mounting different end effectors to the setup (i.e. the spindle and Keyence laser displacement sensor). The overall appearance of the test setup is given in **Error! Reference source not found.**.

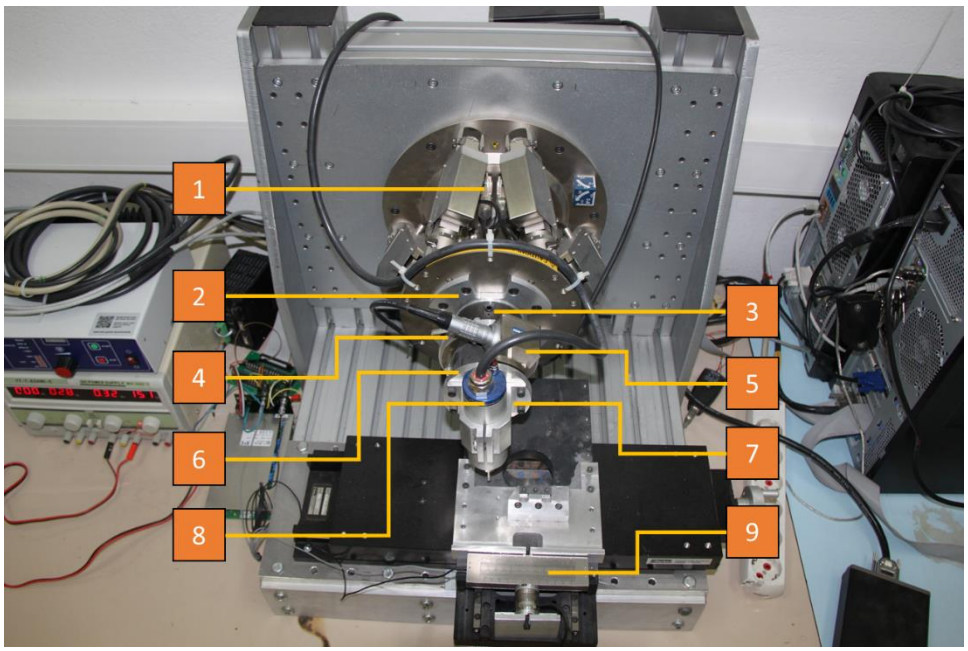

Figure 10 - Overall appearance of the test setup.

The parts list and descriptions are given in **Table 1**. The spindle, laser sensor, force/torque sensor, hexapod and piezo actuator are controlled by the workstation. The laser sensors and piezo actuator are additional capabilities of the setup and are not utilized in this thesis. Libraries for spindle and Keyence are prepared in C++, MATLAB/SIMULINK (for data analysis) as well as in SolidWorks (for laser calibration with point cloud data) environments in order to be resourceful.

Table 1 - Names and purposes of the parts listed in **Figure 10**.

Number	***Name***	***Purpose***
1	*Hexapod parallel manipulator.*	*To accurately position the spindle for accessing work-piece from different positions.*
2	*Hexapod to tool changer connector.*	*Tool changer structure is connected to the Hexapod via this part.*
3	*Tool changer*	*Tool changer is from System 3R. See Section 3.4.1*
4	*Tool changer to Force/Torque sensor connector.*	*Force/Torque sensor is connected to the tool changer via this part.*

Table 1 – (continued)

5	*Force/Torque sensor*	*Force/Torque sensor is from ATI company. See Section 3.3.3*
6	*Tool holder*	*Spindle is a cylindrical object, in order to connect the spindle to the setup, we designed a tool holder that squeezes the spindle via bolts.*
7	*Force/Torque to tool holder connector*	*Tool holder is connected to the setup over Force/Torque sensor (allowing measurements of forces and torques arising in grinding process) over this part.*
8	*Spindle*	*Spindle is from BMR company. See Section 3.3.2*
9	*Piezo actuated stage*	*Piezo actuator is connected to linear stage via two structural elements explained in Section. Work-piece is connected to this stage over connection targets.*
Laser cut connection plates.	*These structures hold the Hexapod and overall setup together.*	
Remaining structural elements are sigma profiles.	*These profiles are basic structural elements connecting the machine.*	

3.3. Main Devices used in the Thesis

The experimental setup consists of three main devices which require special coverage. In the following subsections these three devices are discussed.

3.3.1. Hexapod (Parallel Manipulator)

In fact, the idea of using a parallel manipulator in machining operations is not a new idea. Previously parallel manipulators were used for their exceptional precision in micro-machining or in polishing, etc. The kind of manipulator utilized in this thesis was actually used for astronomy and space science. According to [36], "PI's M-824 Hexapod (almost the same as the one used in this thesis), is selected to construct space

flight hardware for the LISA (Laser Interferometer Space Antenna).” The accuracy of the motion generated by the manipulator, allows decoupling of the error induced by this motion. This proves to be very attractive when it comes to experiments for building models in grinding. The parallel manipulator combined with an industrial serial manipulator seems to be the next stage in robotic grinding/deburring applications. This combination enables both the precision and reachability. For the first step, the parallel manipulator’s adaption to the machining operations is needed. Therefore, the experimental setup presented in this study comes forward. In addition, the combination of the parallel manipulator’s accuracy with the grinding capabilities of the superabrasives, according to the author’s humble opinion, will be very attractive in precision robotic grinding research.

First of all, the parallel manipulator is a 6 axis positioning device. One of the important properties of this device is its pivot point. Pivot point means a virtual point (that can be defined via software) that the manipulator rotates around (the upper plate of the Hexapod (name of the parallel manipulator) moves around this point). Tuning this point changes the impedance of the manipulator; that is important when it comes to the application of force/impedance control on this device. Since the F/T sensor is mechanically connected to the Hexapod, and the spindle forces can be resolved in the reference frame attached to the pivot point, by changing the pivot point, the amount of pressure that the robot applies on the environment can be changed.

Figure 11 - Hexapod H-824 from PI Company [37].

The Hexapod is directly connected to the main frame of the test setup. The tool changer, force/torque sensor, and the spindle are connected to the Hexapod's upper mounting plate via custom built connection adaptors. The Hexapod is shown in **Figure 11**.

3.3.2. Spindle

Spindle is selected based on the following main criteria.

a) Spindle's company must provide its frequency converter with it.
b) Frequency converter must allow direct access to the variables of the spindle (i.e. spindle speed, current, load)
c) Spindle must accompany hall-effect sensors to read true speed value directly without ambiguous calculations.
d) Can be connected to computer via standard RS232 interface.
e) The spindle is required to reach 30000-40000 RPM in normal operation conditions. It must allow reaching 60000 RPM.
f) The weight of the spindle must be below 1 kg.
g) Rated power value must be around 300 Watts.

(a) (b)

Figure 12 - Frequency converter (a) and the spindle (b) from BMR Company.

Based on these requirements, BMR Company's Z42-M160.19 K1S2 Spindle – Frequency Converter bundle is selected (**Figure 12**). This particular spindle can reach up to 60000 RPM (In Appendix A.4 the datasheet of the spindle is provided).

The frequency converter is connected to the workstation over its 15 pin D-SUB connector's RS232 pins and a library for controlling the spindle is developed (Explained in Section 3.5.1)

3.3.3. Multi Axis Force/Torque Sensor

Since the main goal of the thesis is to develop a cutting force model for grinding operations, this sensor is fundamentally the main source of information.

Figure 13 - ATI Gamma F/T sensor.

In the study, this sensor is placed before the spindle, to observe the cutting forces during the process. By doing so, the forces due to the tool holder and the spindle are constantly affecting the readings. Fortunately, these forces can be recorded while in idle mode and the corresponding voltage values can be subtracted from the readings during the operation. This procedure is called biasing.

Based on the following requirements we selected the multi-axis force/torque sensor, ATI Company's GAMMA IP60 model with SI-130-10 calibration (**Figure 13**).

a) Force/torque sensor must withstand the heavy loads (e.g., weight of the parts connected to it; spindle, tool holder, connection plate, and abrasive mounted bits as well as dynamic loads due to grinding/grinding process behavior),
b) It must give a good balance between accuracy and signal-to-noise ratio,
c) Cannot be heavier than 500 gr., must withstand dust (at least IP60).

d) Must be calibrated in factory before shipment, and must be delivered with its calibration data,
e) Must have computer connection via a DAQ that the mechatronics laboratory already have (NI DAQ 6052E)
f) Could be controlled over MATLAB/SIMULINK, C++
g) Its resolution must be around: 1/30 N for force in x and y direction, and 1/600 Nm for torque in x and y directions.

3.4. Additional Setup Devices and Parts

The main body of the experimental setup made out of sigma profiles. The support elements are 10 mm width steel plates cut by laser. The base of the setup has two additional degrees of freedom which are not controlled during the experiments, however will be used in future studies. There are two linear stages that allows these degrees of freedoms. A piezo-electric actuator is mounted to one of the linear stages and provides additional control in Z direction (with respect to Hexapod's reference frame). The other linear stage has a knob that allows manual positioning.

3.4.1. Tool Changer

In order to have a functional test setup, a System 3R manual tool changer and macro pallet along with a drawbar has been bought (**Figure 14**). Tool changer is mounted to the setup and fully functional.

(a) (b) (c)

Figure 14 - Tool changer 3R-600.24-S. (a) and the macro pallet 3R-651.7E-S (b) and 3R-605.2 drawbar (c) from System 3R company.

The spindle and force measurement is important for model development. What is planned as a future work and equally important to have is measuring the surface of the work-piece before and after the grinding process. Measuring the surface of the work-piece after the grinding process is needed for assessing how well the grinding algorithms worked (by looking at the surface quality, or auto-correlation function) and penalizing or rewarding the reinforcement learning algorithm. Measuring the work-piece surface before the grinding is needed because the model for the grinding process will take the surface geometry of the part into account.

The spindle and force/torque sensor are connected to each other and act together. Whereas, measuring the surface profile of the work-piece can be a separate operation. This enables the idea of utilizing a tool changer for different operations.

3.4.2. Piezo Actuated Stage

In this work a P-602 Piezo-Move flexure-guided piezo actuator is placed to control the movements of the table sensitively (**Figure 15**). Its resolution and response time are higher than the Hexapod. It is aimed to adjusting the position of the piezo actuator and obtaining penetration force as an output. Therefore the process time will be decreased and the quality of the work will be increased by providing high resolution and low response time.

Figure 15 - P-602 Piezo-Move flexure-guided piezo actuator

The piezo actuator is controlled by its PI E-610.S0 LVPZT motion amplifier/controller for Strain Gauge sensors which includes PI (Proportional and Integral) controller to provide travel ranges up to 1 millimeter. This controller is designed to be used in closed-loop mode, since the piezo actuator is able to provide position feedback thanks to its strain gauge sensors. As a future work hybrid positioning (a positioning with the contribution of hexapod and piezo actuator) is planned for various grinding tasks and more decreased process times are aimed. Electronic connections between the piezo actuator and the driver is discussed in Appendix D.1.

3.5. The Control Software: Spindle Library, Force/Torque Sensor Library and the Test Bench

Three main devices (Hexapod, force/torque sensor, and spindle) are connected to the workstation over the protocols summarized in **Figure 16**.

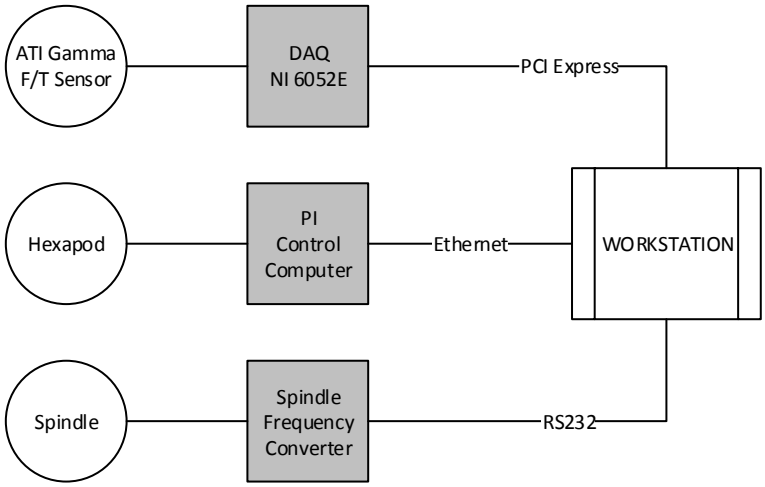

Figure 16 - Devices and connection protocols.

The Hexapod has its separate control computer that runs a UNIX based real-time operating system. This computer has monitor support that shows a user interface when connected.

The experiment starts with the "Start Experiment" button shown in **Figure 17** and the software starts collecting ATI F/T sensor, spindle, and Hexapod data (motion in Z

direction while moving in Y direction). These data are saved as a CSV file and imported with MATLAB for modeling and data analysis.

The data is collected using multi-threaded approach. Since both spindle and F/T data must be collected simultaneously, two separate infinite loops starts when the “Start Experiment” button is clicked. In these infinite loops both spindle and the F/T sensor reads the device data in raw format as soon as possible and repeats that action until “Save Data” button is clicked.

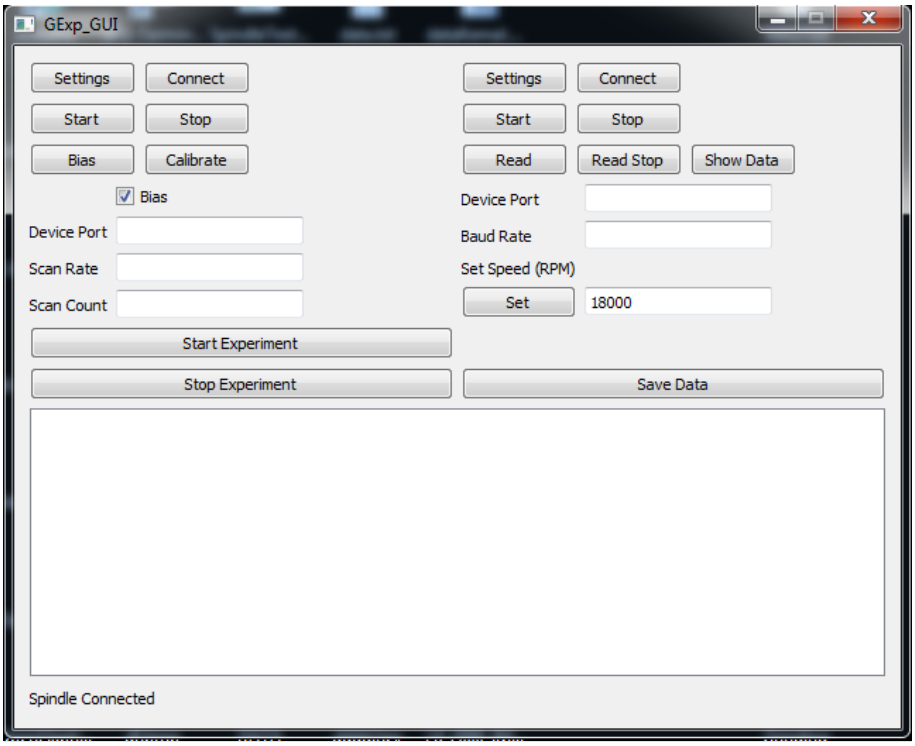

Figure 17 - The "Control Software" spindle and F/T sensor control and measurement section.

The Qt (version 5.4, [38])framework is used for developing the control software. Its elegant *signal()* and *slot()* mechanism and easy to use *QThread()* class allow fast software prototyping .

The Hexapod motion commands for the experiments are submitted using the user interface shown in **Figure 18**. Hexapod is connected to its own control computer, whereas the control computer itself is connected to the workstation over Ethernet

port. The control software reaches to the control computer over the Ethernet port and uses predefined control commands (supplied by the company) to control the Hexapod.

Hexapod's velocity, before any command, must be set. This is achieved by adjusting the velocity from the number box and pressing the move to target button. All 6 axes of the Hexapod is then can be set to the target value and pressed to move to target button again. Then, the Hexapod moves to the specified target with the set velocity.

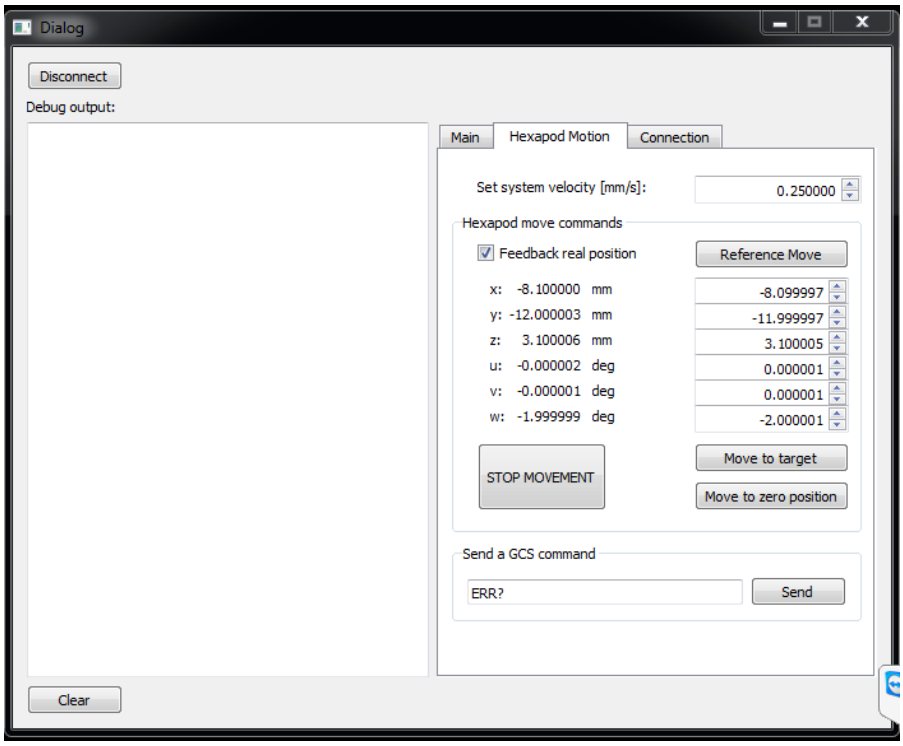

Figure 18 - The "Control Software" - Hexapod control section.

3.5.1. The Spindle Library

Controlling the spindle from the computer is the key for developing the grinding model. The spindle speed is controlled from the computer, and spindle outputs are fed back to the computer and captured by the software. Current and load can be read from the frequency converter of the spindle. The current speed (true speed) can also

be read since the spindle has hall-effect sensors. The spindle library is designed so that we can use the spindle at its full potential.

For RS232 communications Qt's QSerialPort class is used. This class provides industry standard communication methods for cross-platform serial port linking. Qt class structures are easy to use and understand as well as allowing fast prototyping of code. Synchronous communication scheme is adopted for the communication. Spindle Library (SL) is in class structure and consists of two includable files (it was unnecessary to convert the class into static or dynamic library), namely Spindle.h and Spindle.cpp.

A partial spindle class definition is given in **Figure 19**. Its main part is *iRead()* signal and *doRead()* slot. When the spindle class object is created it must be moved to its separate thread in the GUI environment (control software). When the *iRead()* signal is fired, the thread goes into *doRead()* slot and starts reading spindle speed, spindle current, and spindle percent load values. At the end of the *doRead()* slot, the objects emits *iRead()*. This way, it goes into an infinite loop until *iRead()* and *doRead()* connection are disabled. (This is achieved by clicking "Save Data" button in the control software).

```
class spindle : public QObject
{
    Q_OBJECT
public:
signals:
    void iRead(); // Trigger continuous data record.
    void iStopReading(); // Trigger stop reading sequence.
    void iStartReading(); // Trigger start reading sequence.
public slots:
    void doRead(); // Continuous data record.
    void doStopReading(); // Stop reading sequence.
    void doStartReading(); // Start reading sequence.
};
```

Figure 19 - Partial class definition of the spindle library.

The data record sampling time is approximately 10 *ms*. In addition to these core functions, there are methods that starts and stops the spindle, changes the speed of the spindle, and conveys critical information (for instance, the current temperature of the spindle) to the user.

3.5.2. Force/Torque Measurement Library

As in the spindle case, this is also developed as a C++ library using Qt. However, ATI F/T sensor uses National Instrument Data Acquisition Cards (DAQ) for communication with the computer. In order to access to the ATI F/T sensor, NI-DAQ library is used. Again, the object of this class must be moved into its separate thread.

```
class DAQSys : public QObject
{
    Q_OBJECT
signals:
    void iRead(); // this is what triggers reading train.
    void iStop(); // this stops the data reading.
    void iBias(); // signal that triggers reading voltages for biasing later.
    void iCalibrate(bool); // triggers calibration phase.
    void iConverted(); // informs peers successful conversion.
    void iSettings(QString, double, double); // trigger the settings.
public slots:
    // allows GUI communication while "this" is in thread!
    void doRead(); // reads the current data, stores it and emits iRead() again.
    void stopReading(); // does nothing. This is for breaking the data reading train.
    void saveBias(); // save the bias value when the iBias signal is triggered.
    void doCalibrate(bool); // performs calibration.
};
```

Figure 20 - Partial class definition for ATI F/T sensor access library.

A section of ATI F/T class definition is given in **Figure 20**. The class structure of the Force/Torque measurement library consists of DAQSys.h and DAQSys.cpp. Similar

to spindle library it goes into an infinite loop within its thread and reads forces and torques from the sensor as fast as possible (as raw voltages).

Since the test software (main thread) is not running under a real time operating system, the measured data is also accompanied with time stamps in nanoseconds for later accessing the record times. The sampling time of the record is approximately 3 *ms*. The time stamps of the both spindle and force/torque measurement results are used for equal sampling of the two measurements.

CHAPTER 4

PREDICTION OF THE CUTTING FORCES

4.1. General Overview

In grinding process, the force prediction is highly related with geometry of interaction, speed of the wheel, speed of the workpiece (or in robotic grinding, speed of the end-effector), micro cutting action of grits on the wheel, stochastic distribution of grits on the wheel, workpiece material hardness and mechanical properties, usage of coolant, wear on the wheel, dressing condition of the wheel if it is dressed, and material burn [10]. The analysis of the forces due to all these effects is complicated. However, for the same workpiece, by defining a simple geometric interaction and using the same wheel, an experimental force model between the experiments set conditions can be obtained. In this study, the normal and tangential forces are predicted for the same workpiece material, for a well-defined geometry, and for the same wheel. In order to build an experimental force model, 96 (80 penetration tests, 16 additional verification tests) experiments are done. During the experiments, the normal and tangential forces are recorded along with spindle load and current. The multi-axis force-torque sensor provides also additional torque information and the force in radial direction (6 axes sensor).

The experimental setup consists of mainly the Hexapod robot (PI-H-824 6-Axis Parallel Manipulator), F/T sensor (ATI-Gamma-IP60), a high speed spindle (BMR – Z42-M160.19 K1S2), a manual tool changer (System 3R-6**), a piezo-electric actuator (PI-P-602), a custom build frame structure, custom build connection adaptors, workpiece holder (fixture), workpiece, grinding wheel and two linear stages. Note that the tool changer and the piezo-electric actuator are reserved for further research

The penetration experiments are performed as described in Section 4.2.1. For these experiments, the experiment set conditions and the experiment numbers are given in **Table 2**. The peak normal-and tangential forces are listed in **Table 8** in Appendix C.3. The feed-rates can be looked-up from (**Table 2**)

Table 2 - Experiments layout. Experiment numbers are given in parenthesis

	150 µm	*300 µm*	*450 µm*	*600 µm*
10000 RPM	*0.2 mm/s (1)*	*0.2 mm/s (5)*	*0.2 mm/s (9)*	*0.2 mm/s (13)*
	0.4 mm/s (2)	*0.4 mm/s (6)*	*0.4 mm/s (10)*	*0.4 mm/s (14)*
	0.6 mm/s (3)	*0.6 mm/s (7)*	*0.6 mm/s (11)*	*0.6 mm/s (15)*
	0.8 mm/s (4)	*0.8 mm/s (8)*	*0.8 mm/s (12)*	*0.8 mm/s (16)*
12500 RPM	*0.2 mm/s (17)*	*0.2 mm/s (21)*	*0.2 mm/s (25)*	*0.2 mm/s (29)*
	0.4 mm/s (18)	*0.4 mm/s (22)*	*0.4 mm/s (26)*	*0.4 mm/s (30)*
	0.6 mm/s (19)	*0.6 mm/s (23)*	*0.6 mm/s (27)*	*0.6 mm/s (31)*
	0.8 mm/s (20)	*0.8 mm/s (24)*	*0.8 mm/s (28)*	*0.8 mm/s (32)*
15000 RPM	*0.2 mm/s (33)*	*0.2 mm/s (37)*	*0.2 mm/s (41)*	*0.2 mm/s (45)*
	0.4 mm/s (34)	*0.4 mm/s (38)*	*0.4 mm/s (42)*	*0.4 mm/s (46)*
	0.6 mm/s (35)	*0.6 mm/s (39)*	*0.6 mm/s (43)*	*0.6 mm/s (47)*
	0.8 mm/s (36)	*0.8 mm/s (40)*	*0.8 mm/s (44)*	*0.8 mm/s (48)*
17500 RPM	*0.2 mm/s (49)*	*0.2 mm/s (53)*	*0.2 mm/s (57)*	*0.2 mm/s (61)*
	0.4 mm/s (50)	*0.4 mm/s (54)*	*0.4 mm/s (58)*	*0.4 mm/s (62)*
	0.6 mm/s (51)	*0.6 mm/s (55)*	*0.6 mm/s (59)*	*0.6 mm/s (63)*
	0.8 mm/s (52)	*0.8 mm/s (56)*	*0.8 mm/s (60)*	*0.8 mm/s (64)*
22500 RPM	*0.2 mm/s (65)*	*0.2 mm/s (69)*	*0.2 mm/s (73)*	*0.2 mm/s (77)*
	0.4 mm/s (66)	*0.4 mm/s (70)*	*0.4 mm/s (74)*	*0.4 mm/s (78)*
	0.6 mm/s (67)	*0.6 mm/s (71)*	*0.6 mm/s (75)*	*0.6 mm/s (79)*
	0.8 mm/s (68)	*0.8 mm/s (72)*	*0.8 mm/s (76)*	*0.8 mm/s (80)*

During the experiments 4-mm radius electroplated, mono-layer nickel bonded cBN wheels (PFERD 4, 0-5/3-45 B126) are used (see **Figure 21**). In the manufacturer's catalog [39], the nickel layer size was given as half of the average grit size. For these

wheels, the average grit size was indicated by B126 and corresponds to 126 μm. Therefore the minimum penetration depth is set to 150 μm. The maximum penetration depth is set according to the forces obtained from preliminary experiments to 600 μm.

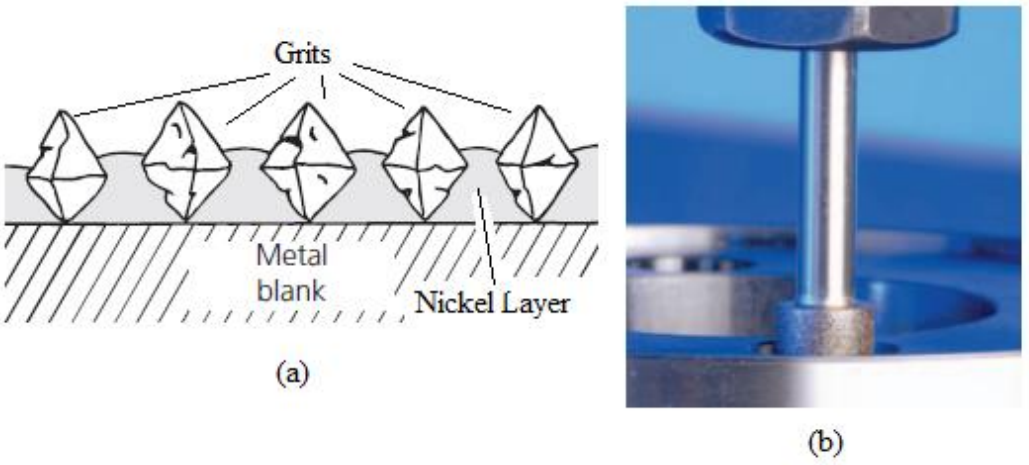

Figure 21 - cBN wheel surface profile (a). cBN wheel appearance (b). [39]

During the experiments, a very narrow range of operation is considered for the spindle speed (10000 RPM – 22500 RPM). From the manufacturer's catalog it can be found that for this cBN wheel, rotational speeds can be as high as 70000 RPM. Spindle in the experimental setup also has high speeds (max 60000 RPM). Therefore, a typical spindle speed region for this study would have been 40000 RPM – 60000 RPM. The tests in this thesis are done at much lower spindle speeds (10000 RPM – 22500 RPM) and can be repeated for the 40000 RPM - 60000 RPM region.

In **Figure 22**, for different spindle speeds, five polynomial curve fits are shown. For low depth of cut and feed rate, change in the spindle speed does not affect the normal force considerably. Similar behavior can be observed for high feed rate low depth of cut and high depth of cut low feed rate. However, for high depth of cuts and high feed rates, spindle speed affects the normal forces significantly. Increasing the spindle speeds make the process more efficient and reduces the forces. In this operation region, for an efficient operation spindle speed must be high. Therefore, in order to work in this region it is best to set the spindle speed to 22500 RPM, or more.

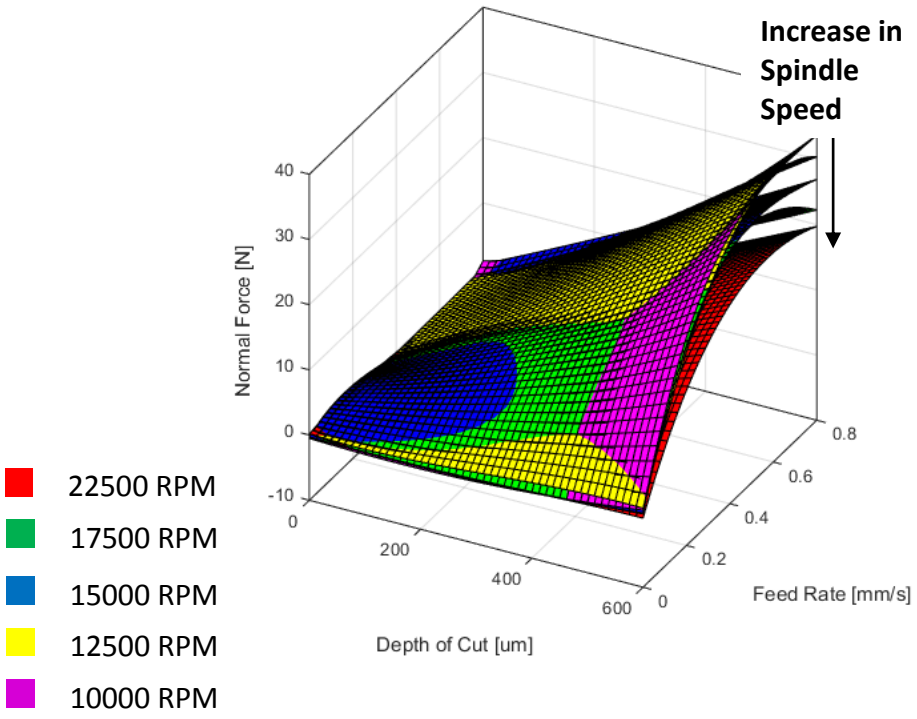

Figure 22 - Process chart. Effect of spindle speed on the normal force.

The process chart shows parameter effects on the normal force but the behavior is same for the tangential force. The tangential force and normal force during the penetration tests are almost equal to each other. In tangential (lateral) grinding normal force peak value is same as the penetration test peak normal force value for the same grinding process parameters. However, in tangential grinding the tangential force must be calculated by normal force and friction coefficient. The friction coefficient is a function of almost all of the grinding operation parameters. Thus, prediction of the tangential force in tangential surface grinding is difficult. This is one of the reasons that the penetration tests are more suitable for modeling the grinding operation for robotic grinding studies. The model developed based on penetration experiments predicts the normal force for both penetration and tangential surface cutting cases. This is why penetration tests are valuable. It provides more controlled study of the normal force. Besides, the normal force is more important for a force/impedance based controller design.

Change of contact surface during the experiments is not too high in penetration tests, however as can be seen from **Figure 28** and **Figure 29**, in tangential surface grinding, normal and tangential forces are quite different.

4.2. Experiments

The experiments are done in the experimental setup explained in **Error! Reference source not found.**. In this section, the experiments are explained. In order to obtain the cutting forces for modeling, the workpiece is fixed to a fixture as shown in **Figure 23**.The fixture material is Aluminum (7075) and the workpiece material is St37. The workpiece is fixed onto the fixture via three M3 bolts (from the connection points shown in **Figure 23**). Also the fixture provides an osculation surface to prevent workpiece motion due to loosen bolts (even though the bolts are affixed by applying a Loctite glue, they could still allow small motions).

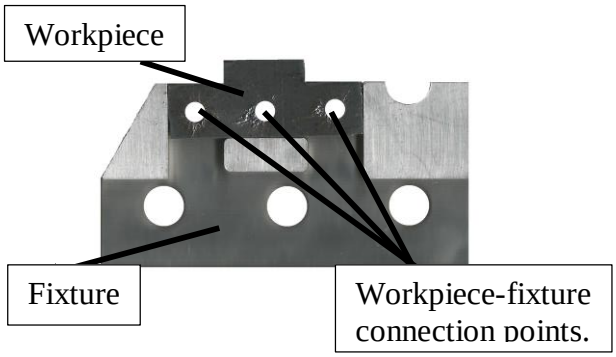

Figure 23 - Workpiece fixture and workpiece in position.

The fixture is placed on top of the fixture holder and bolted via M6 bolts. The workpiece edge is 1 mm near the wheel position when the hexapod is at its reference point (origin). When the workpiece has no surface to cut, it is removed from the fixture and new workpiece is mounted.

In the experiments, a manual collet (ER11) is used to connect the cBN wheel to the spindle. This collet does not allow cBN wheel root height adjustment. Therefore, the cBN root size inside the spindle changes at each time a new tool is mounted.

Therefore when a new tool is mounted, the hexapod must position the tool accordingly (with respect to the workpiece).

Hexapod positions the cBN wheel near the workpiece as shown in **Figure 24** for initial surface preparation. The spindle starts rotating around 17500 RPM and the Hexapod moves the cBN wheel almost perfectly (with a 1 μm error in –Z direction) in the +Y direction. This operation removes the surface shown as the orange line in **Figure 24** with 3 passes. After 3 passes the cutting forces disappear and surface becomes ready for penetration tests. Since neither the workpiece surface nor the tool or Hexapod orientation are perfectly perpendicular, initially, this operation prepares a perpendicular surface for the cBN wheel to perform penetration tests. The reference system shown by red lines are the reference system imposed by the force/torque sensor.

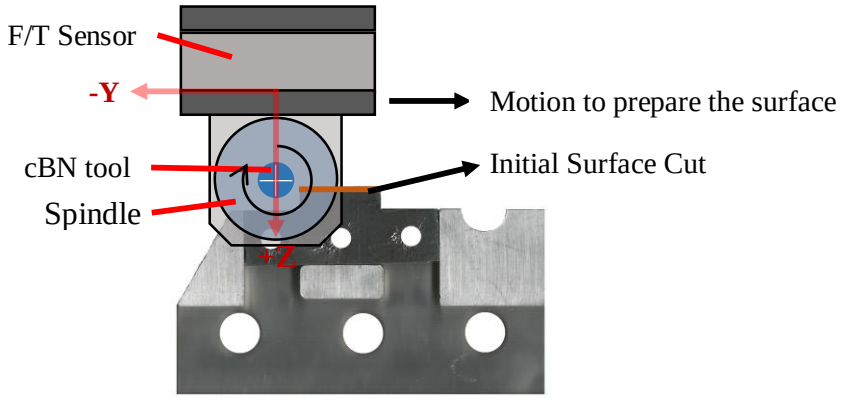

Figure 24 - Initial surface preparation.

During the experiments the spindle may warm up. Because of change in the spindle temperature, the experiments are done by waiting 10 minutes between each experiment (there is a temperature sensor on spindle, and each experiment started at the same idle temperature of the spindle).

4.2.1. Penetration Experiments

The penetration tests (all 80 experiments 3 by 3) always start with the surface preparation. After the surface preparation the tool can penetrate the workpiece from

3 points (because of the workpiece width) as shown in **Figure 25**.When the tool cuts through the workpiece it does not cut the material instantly. Therefore the wheel root starts deflecting. When the Hexapod reaches the set depth of cut (SDOC), it is set to stay there for a while to observe zero cutting forces in measurements. For an example of the force profile please refer **Figure 30**.

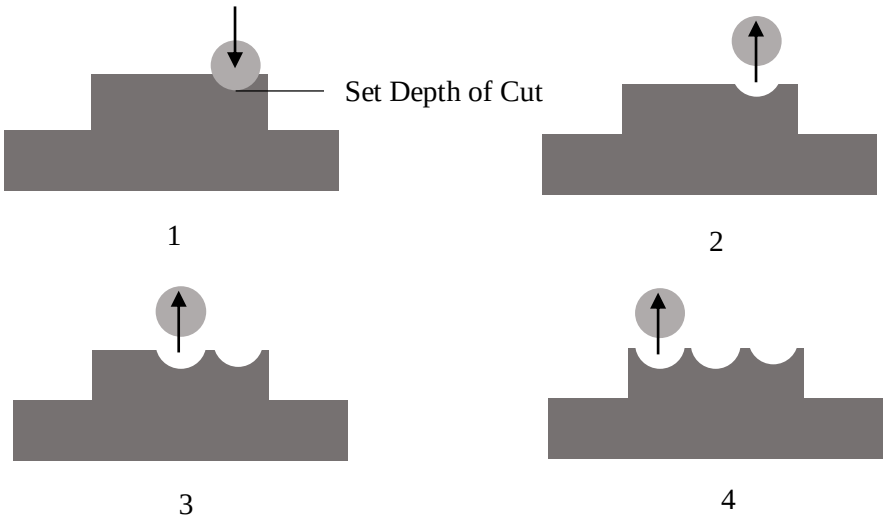

Figure 25 - Set depth of cut (SDOC) and 3 consecutive penetrations for initialized surface.

The workpiece after 3 penetrations is shown in **Figure 26**. The part finishes after 15 penetrations (meaning 15 experiments).

(a) *(b)*

Figure 26- Workpiece after penetrations. Up (a) and side (b) views.

4.2.2. Verification and Experiment Consistency Tests

In order to verify and check the consistency of the experiments, additional tests were done (16 experiments) including penetration and tangential motion. 8 out of the mentioned 16 experiments were dedicated to arbitrary spindle speeds, set depth of cuts, and feeds within the region where the penetration tests were done. This data set was used to test the model accuracy. The remaining 8 experiments are the repetition of 8 experiments in the penetration tests. 5 experiments out of the 8 showed almost the same pattern. The summary of the 16 additional experiments can be found in the below **Table 3**.

Table 3 - Model verification and experiment consistency tests.

10000 RPM		*12500 RPM*		*15000 RPM*		*17500 RPM*	
300µm	*0.6mm/s*	*300µm*	*0.6mm/s*	*300µm*	*0.6mm/s*	*300µm*	*0.6mm/s*
450µm	*0.6mm/s*	*450µm*	*0.6mm/s*	*450µm*	*0.6mm/s*	*450µm*	*0.6mm/s*
500µm	*0.7mm/s*	*500µm*	*0.7mm/s*	*450µm*	*0.7mm/s*	*450µm*	*0.7mm/s*
500µm	*0.5mm/s*	*500µm*	*0.5mm/s*	*450µm*	*0.5mm/s*	*450µm*	*0.5mm/s*

VEC tests is used for verification of the neural network model given in Section 3.4. The experiment procedure is summarized in **Figure 27**. During the VEC tests, two separate motions are considered. The penetration part of the VEC is used for both model verification and checking the consistency of the previously done experiments (80 penetration tests). The tangential cutting part is used for finding the ADOC given the grinding operation parameters.

In **Figure 27**, the VEC starts with a regular penetration test (as explained in the previous subsection) and shown by (1). The second part shows a tangential motion. When the tool reaches to the target point (3) it stays there until forces disappear. In (4) the wheel moves upward and away from the part.

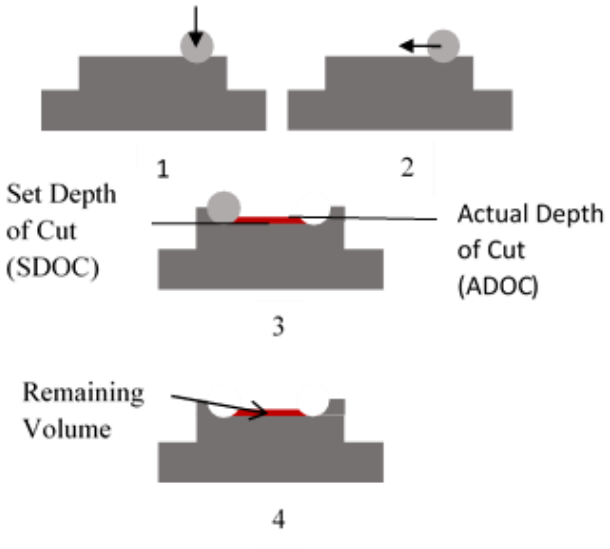

Figure 27 - The procedure followed during the VEC (Verification and Experiment Consistency) tests.

A volume remains because of the grinding factors (machine stiffness, cutting stiffness, dynamic characteristics of the machine and the operation conditions).

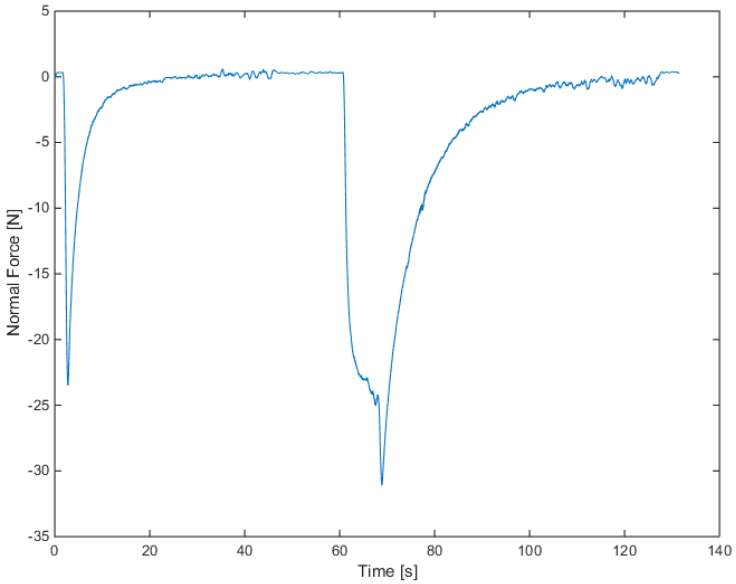

Figure 28 – Example of normal force pattern from VEC data-set (12500 RPM, 450 μm, 0.6 mm/s).

In **Figure 28** and **Figure 29**, the first force profile shows the penetration part. The force dies out after a while. Then the tangential motion takes place. During the tangential motion, the normal force also makes another peak when the tool reaches to the target position because of the up-cut effect. The tangential force pattern for the same experiment shows a different pattern. It stays stable (stable tangential cutting) for a while.

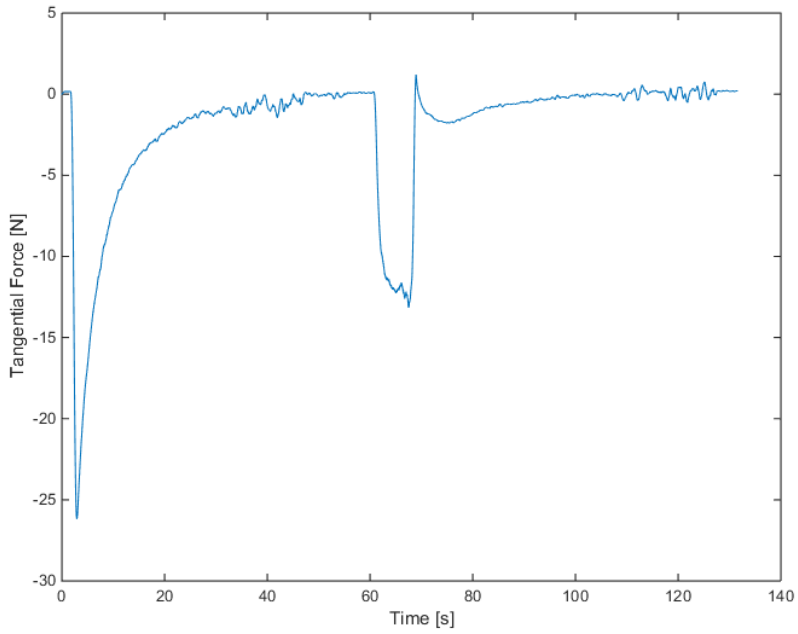

Figure 29 - Example of tangential force pattern from VEC data set. (12500 RPM, 450 μm, 0.6 mm/s).

4.3. Penetration Test Typical Force Profile and Friction Behavior

In penetration experiments the tangential and normal forces follows the same force profile. This makes analysis of the process properties easier. The force profile for the 36th experiment is provided in **Figure 30**.This experiment is done by setting spindle speed to 15000 RPM, SDOC to 600 μm and feed rate to 0.8 mm/s. When the Hexapod reaches to the SDOC the peak forces occur. During the penetration the tool bends and lags behind the motion of the Hexapod because of the finite stiffness of the system. In the figure, a difference in normal and tangential forces is emphasized. This

behavior is due to the increase in surface area during penetration. Increased surface area means higher friction and tangential force varies with the change in the friction coefficient. It is observed that for high SDOCs this difference is more obvious. The friction coefficient is defined as $\mu = F_t/F_n$. The change in friction coefficient up to the peak points remains constant and almost always 1. However, shortly before the force peaks, friction coefficient tends to increase. This effect is included in neural network force prediction since we both normal and tangential forces are fed to the Network during the training. Therefore, both normal and tangential forces and friction coefficient (calculated using the predicted normal and tangential forces) comes out of neural network as outputs

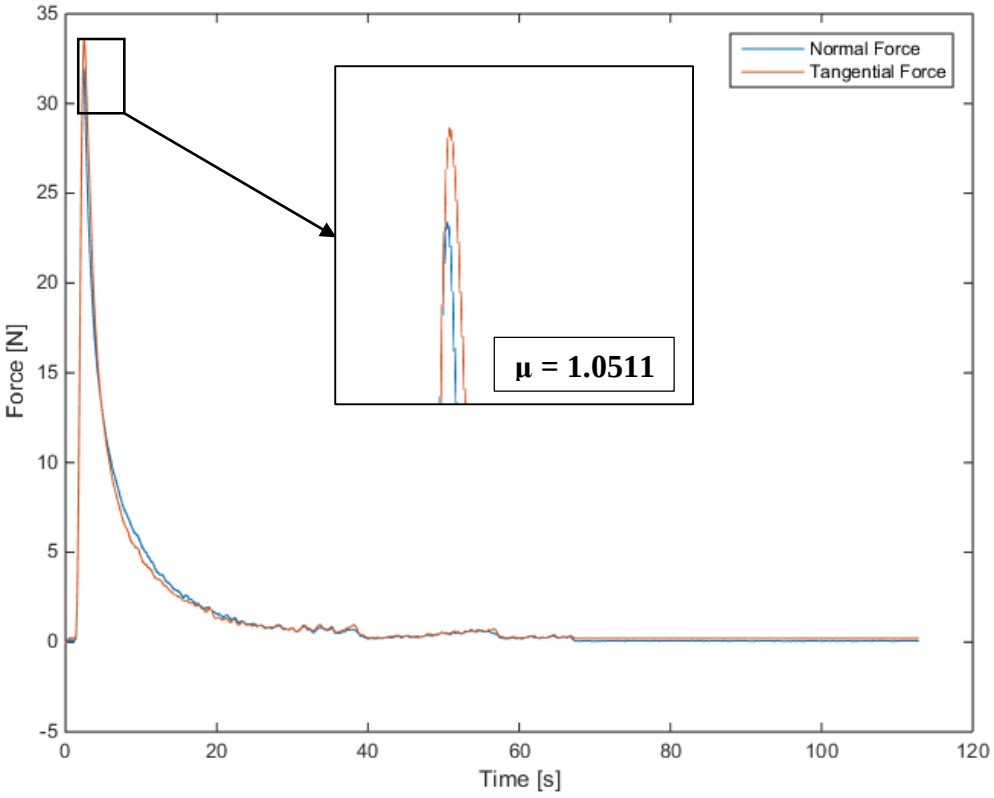

Figure 30 - Normal and tangential force profiles for experiment 36.

4.4. ANN Model

Previously in this chapter, the polynomial approach was discussed. In order to see the effect of spindle speed change, 5 polynomial curve fits were obtained using the MATLAB's curve fitting toolbox. For each spindle speed 16 data points were present. This 16 data points were provided to the curve fitting toolbox and the results were the polynomial parameters. The curves showing the polynomial fits for each spindle speeds were shown in **Figure 22**. But, unlike simple curve fitting, ANN provides multi-dimensional input to output mappings. Using ANN all the effects of the inputs can be seen on the forces. In this section ANN training method is discussed, moreover the simple mathematical definition of how ANN works is also discussed.

The penetration tests are intended to obtain a clean idea about the process and the findings can be used as the force prediction model for the process. The penetrations give cleaner force patterns than tangential cutting (a tangential cutting example force pattern was given in **Figure 28**). In each experiment, the machine and cutting dynamics are also recorded (**Figure 30**). This information provides a better understanding of the process. However, for the given SDOC, only the peak forces are utilized in the model.

The modeling of the process is considered as the prediction of the peak normal and tangential forces. A data table collecting all 80 experiments' peak normal and tangential forces are organized as an array in MATLAB by using simple MATLAB scripts. This array is used as the target data set in model fitting.

The method used for the training of this network was simple back propagation provided by MATLAB Neural Network toolbox. Our outputs are the normal and tangential forces in penetration tests. Friction coefficient can be calculated based on the normal and tangential force.

In the present work, we used multilayer perceptron neural network, for cutting force prediction. Our model is based on the MATLAB's Neural Network Toolbox. The neuron connection architecture is provided in **Figure 31**. 10 neurons are utilized in

the hidden layer. Since the neurons in the hidden layer changes the complexity of the model, we found out by trial and error, 10 neurons in the hidden layer yields the best result.

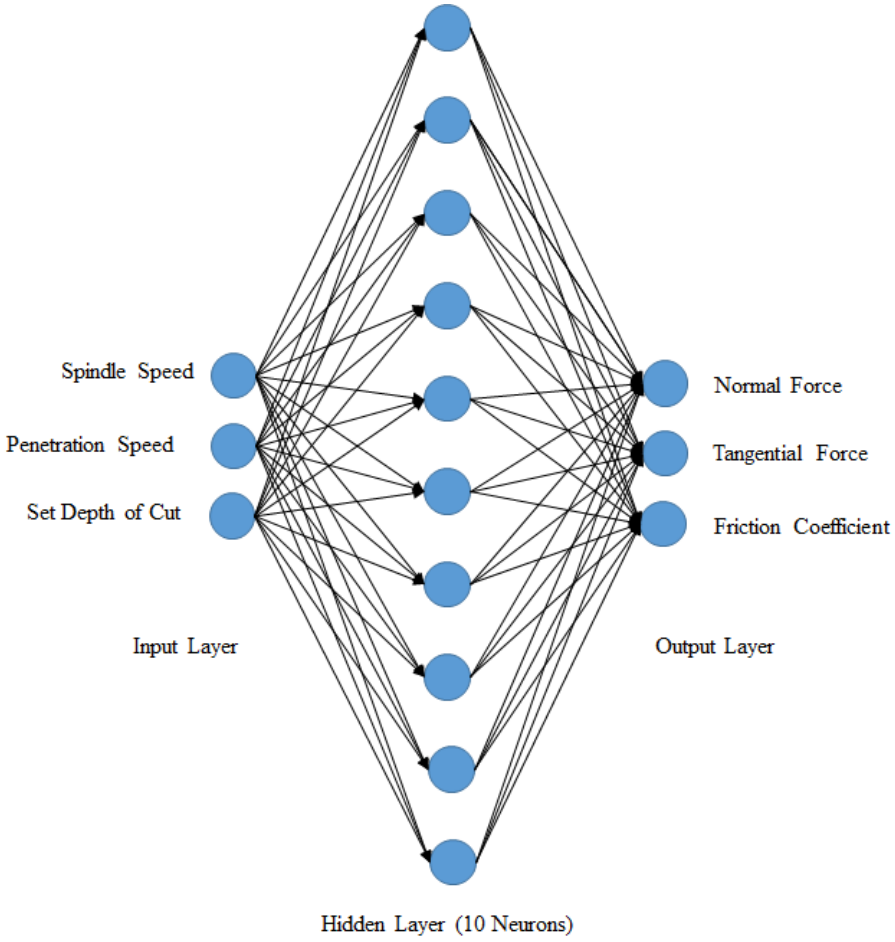

Figure 31 - Multilayer Neural Network Architecture.

In order to determine appropriate weights for the connections and adjust our multilayer perceptron network which is an accurate predictor for such modeling purposes, we chose error back propagation learning method [17], [22].

We used sigmoid function in neurons that is a commonly used function in neural networks terminology, because that is a differentiable function and suitable for gradient descent which is a standard mathematical optimization algorithm and

foundation of back propagation approach. There are other commonly utilized activation functions, such as tangent hyperbolic and log-sigmoid functions.

Figure 32 shows the sigmoid function and it is defined as follow:

Sigmoid function: $f(x) = \frac{1}{(1+e^{-x})}$

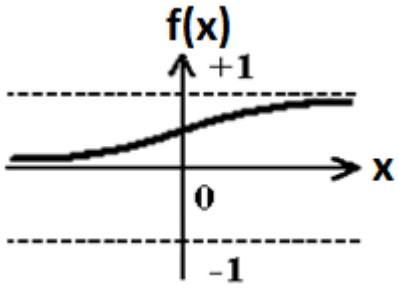

Figure 32 - Sigmoid function.

The important factor for training the MLP is to minimize the squared error of the network's output which is formulated as follow:

$$E = \frac{1}{2}\left(y - f(x)\right)^2 \qquad (6)$$

Where y means the sample's target and $f(x)$ is the network's output prediction value.

Gradient descent is an iterative optimization procedure which is used for adjusting the function's parameters. It takes the value of the derivative, multiplies it by a small constant called the learning rate, and subtracts the result from the current parameter value. This process is iteratively keeps on until reaching a minimum value.

The learning rate means the rate of convergence in learning procedure. The very large value of learning rate for an error function with several minima may lead to overshooting and missing a minimum entirely or wide oscillation and too small value for learning rate may lead to slow convergence of error function to minimum value.

In order to determine the correct weights for a multilayer perceptron, we should compute the derivative of the squared error with respect to each weight in our network.

For output layer, differentiating the error function with respect to each incoming weights w_i yields,

$$\frac{dE}{dw_i} = \big(y - f(x)\big)\frac{df(x)}{dw_i} \tag{7}$$

in which, $f(x)$ means the output value of the perceptron and x means the sum of inputs. Each of them is multiplied by its own weight,.

When we use sigmoid function, the derivative term of function can be expressed in a simple form as follow:

$$\frac{d\,f(x)}{dx} = f(x)\big(1 - f(x)\big) \tag{8}$$

But we want to compute the derivative with respect to w_i, not x, because

$$x = \sum_i w_i a_i \tag{9}$$

So derivative with respect to w_i is

$$\frac{df(x)}{dw_i} = f'(x)a_i \tag{10}$$

Putting Equation (10) in the error function gives,

$$\frac{dE}{dw_i} = \big(y - f(x)\big)f'(x)a_i \tag{11}$$

This formula gives all requirements for calculating the change of weight w_i.We iteratively do this computation for each instance and add the changes with special

weight w_i which is multiplied by learning rate, and subtract the result from w_i's current value.

Regarding hidden layers, the computations keep on as follow. If we consider $f(x_i)$ as the output of i[th] hidden neuron, and w_{ij} as the connection weight from input j to the i[th] hidden neuron and w_i as the weight of i[th] hidden neuron to the output neuron and take the w_i as the weight of the i[th] hidden neuron to the output neuron like, the only change that should be made regarding Equation (11) is replacement of $a_i$with $f(x_i)$ that is the output of i[th] hidden neuron.

$$\frac{dE}{dw_i} = \big(y - f(x)\big) f'(x) f(x_i) \tag{12}$$

Also for correcting the weights w_{ij}, we should calculate the related derivatives using chain rule.

$$\frac{dE}{dw_{ij}} = \frac{dE}{dx}\frac{dx}{dw_{ij}} = \big(y - f(x)\big) f'(x) \frac{dx}{dw_{ij}} \tag{13}$$

The first two terms of the Equation (12) are the same as Equation (13). To determine the last term, the following computations are done.

$$x = \sum_i w_i f(x_i) \tag{14}$$

$$\frac{dx}{dw_{ij}} = w_i \frac{df(x_i)}{dw_{ij}} \tag{15}$$

Moreover,

$$\frac{df(x_i)}{dw_{ij}} = f'(x_i)\frac{dx_i}{dw_{ij}} = f'(x_i) a_i \tag{16}$$

Finally regarding the above equations, the error function with respect to the weights w_{ij} is equal to:

$$\frac{dE}{dw_{ij}} = \big(y - f(x)\big) f'(x) w_i f'(x_i) a_i \qquad (17)$$

Like the previous equations, the above value is calculated for all instances and adds up the changes associated with a particular weight w_{ij}, multiplied by the learning rate, and subtracts the outcome from the current value of w_{ij}.

Because of such error propagation procedure, this algorithm is named back propagation method.

A code has been developed using the above algorithm but was not tested on the real data set. This will be done as a future work and other modeling algorithms will be combined with this lean form of the ANN. For a preliminary analysis after building the actual experimental setup, MATLAB's Neural Network Toolbox is utilized instead.

4.5. Model Verification

Using the VEC data set, the neural network trained using the 80 penetration tests are verified. The verification is done both qualitatively and quantitatively.

The Neural Network toolbox of the MATLAB provides a user interface from which the inputs, targets, and percentages of data utilization (for verification, testing and modeling) can be adjusted. The neuron structure and the number of hidden neurons are then provided. The toolbox, after finishing the mapping, can export the structure as a Simulink file for further testing.

After several trial and errors, a network with 10 hidden neurons in the hidden layer is selected. A better approach to tune the model parameters with genetic algorithm can be found in [40] and [41].

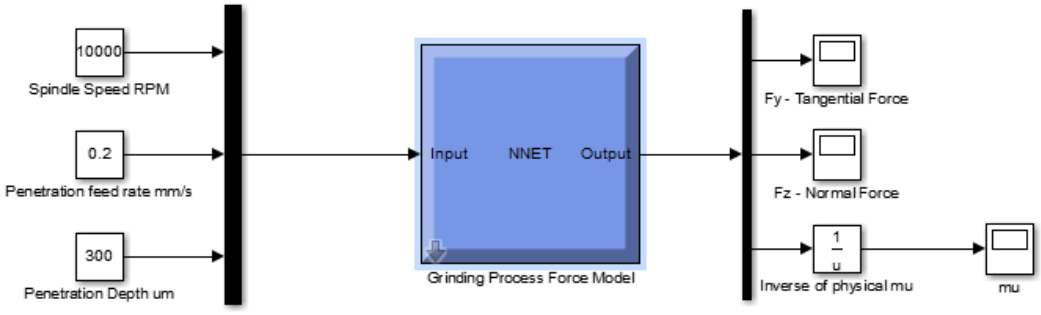

Figure 33 - Neural Network Model in Simulink.

The Neural Network is first exported to SIMULINK environment (**Figure 33**). Then the force peak values are collected (the mapping is done based on **Figure 34**).

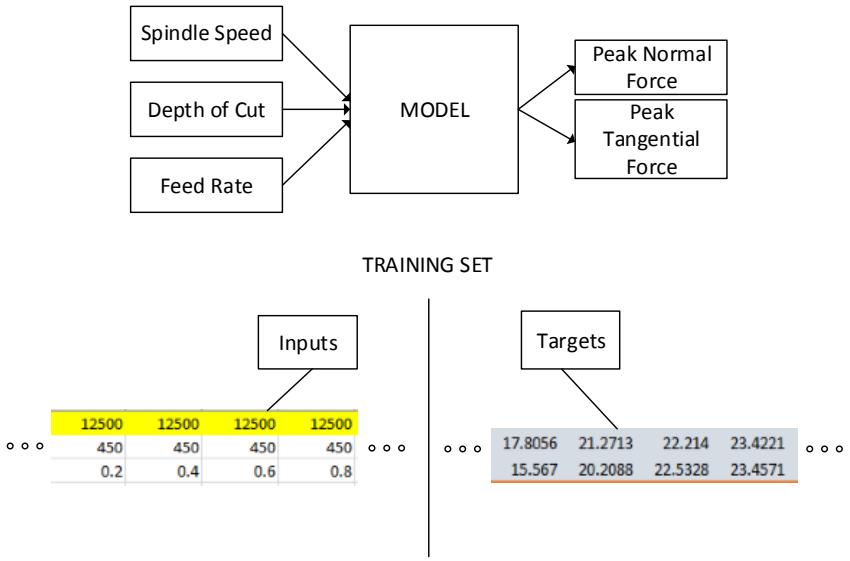

Figure 34 - ANN inputs and outputs. Shows numerical values for the inputs and outputs for some of the experiments.

The model behavior for VEC experiments' depth of cuts, spindle speeds and penetration feed-rates is tested by providing the VEC inputs to the network by using the SIMULINK model shown in **Figure 33**.

In **Table 4** the prediction errors for VEC data set are shown. The errors are mostly under % 10. Due to the need for repetition of the high prediction error experiments, generalization is not fully achieved. However, for 12 experiments out of 16, shows errors around 10 %. The maximum errors are observed in 15000 RPM cases. These are %12.07, %15.32 and %17.64.

Table 4 - ANN model prediction errors for VEC data-set.

Normal Forces	***Normal Forces***	***Normal Forces***	***Normal Forces***
14.77 Actual	*14.21 Actual*	*13.76 Actual*	*13.36 Actual*
13.83 Predicted	*13.57 Predicted*	*12.86 Predicted*	*12.5 Predicted*
Condition	***Condition***	***Condition***	***Condition***
10000 RPM	*12500 RPM*	*15000 RPM*	*17500 RPM*
0.6 mm/s	*0.6 mm/s*	*0.6 mm/s*	*0.6 mm/s*
300 µm	*300 µm*	*300 µm*	*300 µm*
Normal Forces	***Normal Forces***	***Normal Forces***	***Normal Forces***
25.93 Actual	*23.49 Actual*	*22.36 Actual*	*21.9 Actual*
22.52 Predicted	*21.76 Predicted*	*20.46 Predicted*	*19.69 Predicted*
Condition	***Condition***	***Condition***	***Condition***
10000 RPM	*12500 RPM*	*15000 RPM*	*17500 RPM*
0.6 mm/s	*0.6 mm/s*	*0.6 mm/s*	*0.6 mm/s*
450 µm	*450 µm*	*450 µm*	*450 µm*
Normal Forces	***Normal Forces***	***Normal Forces***	***Normal Forces***
30.49 Actual	*27.87 Actual*	*27.5 Actual*	*18.8 Actual*
25.82 Predicted	*24.86 Predicted*	*22.65 Predicted*	*21.38 Predicted*
Condition	***Condition***	***Condition***	***Condition***
10000 RPM	*12500 RPM*	*15000 RPM*	*17500 RPM*
0.7 mm/s	*0.7 mm/s*	*0.7 mm/s*	*0.7 mm/s*
500 µm	*500 µm*	*500 µm*	*500 µm*
Normal Forces	***Normal Forces***	***Normal Forces***	***Normal Forces***
26.02 Actual	*22.05 Actual*	*21.1 Actual*	*20.49 Actual*
24.97 Predicted	*24.26 Predicted*	*23.15 Predicted*	*22.07 Predicted*
Condition	***Condition***	***Condition***	***Condition***
10000 RPM	*12500 RPM*	*15000 RPM*	*17500 RPM*
0.5 mm/s	*0.5 mm/s*	*0.5 mm/s*	*0.5 mm/s*
500 µm	*500 µm*	*500 µm*	*500 µm*

As the final work a 1000 µm depth of cut is given to the Network for 17500 RPM, 0.2 mm/s. The peak normal force calculated by the Network is 26.9 and the actual force obtain from this additional test is 27.68 N. The force variation is less than 1 N (which is fairly reasonable since the 1000 µm input to the system is outside the training region). The same depth is given via a ramp input also to see the force increase pattern. The result is shown in **Figure 35**. Since the region is outside of the training data-set, a constant value is present after the peak point. However, the network finds out the force value as intended for 400 µm difference from the nearest data point in the penetration data-set.

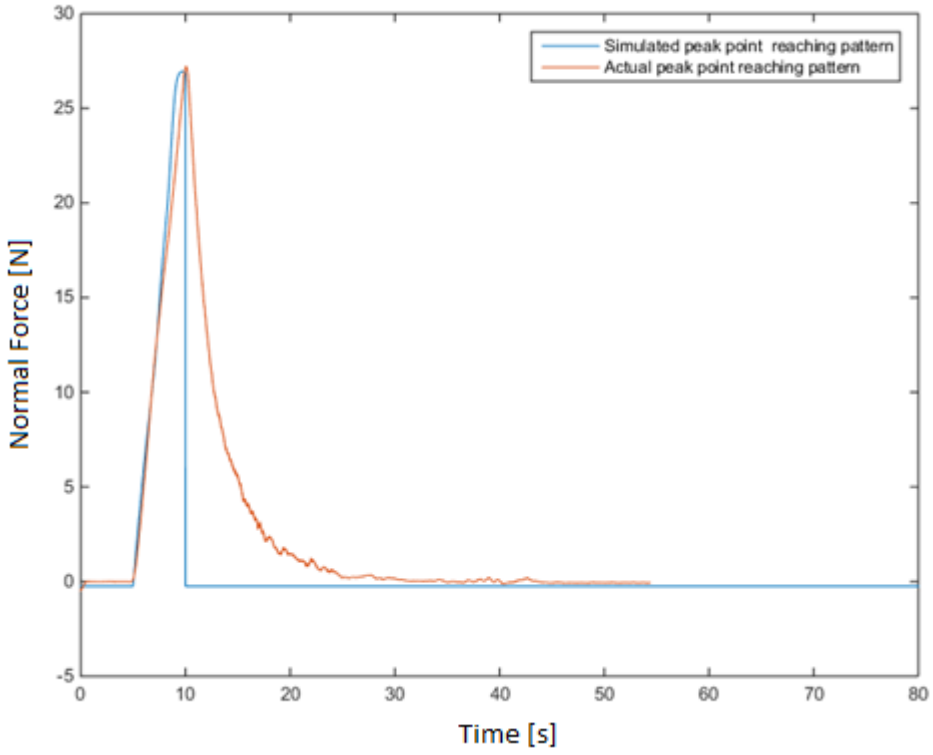

Figure 35 - Force profile for a ramp input. The simulated force pattern is shown in blue. Since the neural network does not deal with the dynamics, the damped profile is not obtained.

CHAPTER 5

KINEMATIC CALCULATIONS OF THE OFFSET IMPOSED BY MOUNTING THE SPINDLE

In order to control the tool position and orientation, the kinematics of the extra links, force/torque sensor, spindle and tool holder should be investigated. In ideal condition it is possible to assume an L-shaped link offset connected to the top plate of hexapod and modify the kinematics with respect to this offset. But, while connecting the spindle to the holder, two small errors should be taken into account. The first one is small roll rotation about Z axis that we call it as φ and the second smal pitch rotation about Y axis that we call it as ζ (**Figure 36**). Both of these errors are modeled in tool kinematics.

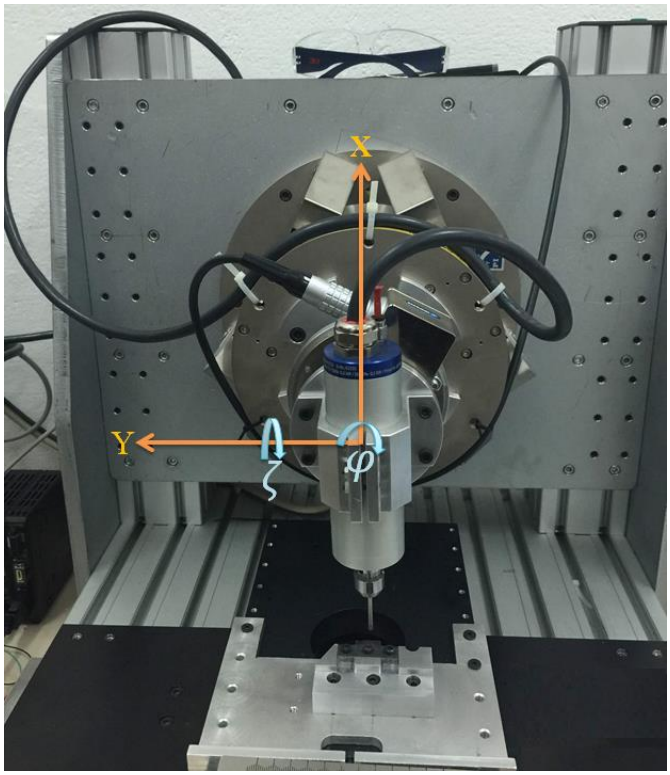

Figure 36 - The errors φ and ζ are mentioned on Hexapod and tool setup.

In this section the offset between the Hexapod plate and the tip-point of the tool is calculated. Such offset needs to be known in order to be able to find the actual commands to be given to the hexapod controller for desired postures and locations of the tip-point.

Starting with the attached parts with the hexapod plate, namely, manual tool changer, tool holder, mounting plates, tool changer adapter and spindle, the dimensions of all these parts are well known and can be found in their technical drawings. Hence, by assuming such parts are rigid the offset can be considered fixed and is calculated as follows

Firstly, the homogenous transformation matrix between the hexapod origin and the plate can be directly found from hexapod's feedback system. Noting that 1-2-3 sequence is used by its controller, the matrix can be written as

$$C^{(p,0)} = \begin{bmatrix} 1 & 0 & 0 \\ 0 & \cos\alpha & -\sin\alpha \\ 0 & \sin\alpha & \cos\alpha \end{bmatrix} \begin{bmatrix} \cos\beta & 0 & \sin\beta \\ 0 & 1 & 0 \\ -\sin\beta & 0 & \cos\beta \end{bmatrix} \begin{bmatrix} \cos\gamma & -\sin\gamma & 0 \\ \sin\gamma & \cos\gamma & 0 \\ 0 & 0 & 1 \end{bmatrix}$$

Then,

$$H_0^p = \begin{bmatrix} & C^{(p,0)} & & x_0 \\ & & & y_0 \\ & & & z_0 \\ 0 & 0 & 0 & 1 \end{bmatrix}$$

Next, add the offset created by the manual tool changer, mounting plates and the tool changer adapter. The offset created by these parts are actually only in the z-direction relative to the plate of the hexapod. That is,

$$H_p^1 = \begin{bmatrix} & I & & 0 \\ & & & 0 \\ & & & L_1 \\ 0 & 0 & 0 & 1 \end{bmatrix}$$

Where L_1 is the relative net offset of the parts mentioned above with the plate, in the z-direction of the plate. Then, adding the effect of the tool holder part, which consists of a translation offset in the same direction of L_1, call it L_2, and a rotation offset around the z-direction of the plate, φ

$$H_1^2 = \begin{bmatrix} & e^{\tilde{u}_3\varphi} & & \begin{matrix}0\\0\\L_2\end{matrix} \\ 0 & 0 & 0 & 1 \end{bmatrix}$$

Lastly, the effect of the spindle can be modeled as if it's a prismatic joint, the reason is that the tool attached to the spindle can be changed and hence its length is not fixed for all tools. Such value will be referred to as p. Also, note that a rotation offset imposed from the tool holder which its effect is noticed at this part, such offset is in the y-axis of the last frame,

$$H_2^3 = \begin{bmatrix} & e^{\tilde{u}_2\zeta} & & \begin{matrix}-p\\0\\0\end{matrix} \\ 0 & 0 & 0 & 1 \end{bmatrix}$$

The overall homogenous transformation from the base frame to the tip-point frame is then

$$H_0^3 = \begin{bmatrix} & C^{(p,0)} & & \begin{matrix}x_0\\y_0\\z_0\end{matrix} \\ 0 & 0 & 0 & 1 \end{bmatrix} \begin{bmatrix} & I & & \begin{matrix}0\\0\\L_1\end{matrix} \\ 0 & 0 & 0 & 1 \end{bmatrix} \begin{bmatrix} & e^{\tilde{u}_3\varphi} & & \begin{matrix}0\\0\\L_2\end{matrix} \\ 0 & 0 & 0 & 1 \end{bmatrix} \begin{bmatrix} & e^{\tilde{u}_2\zeta} & & \begin{matrix}-p\\0\\0\end{matrix} \\ 0 & 0 & 0 & 1 \end{bmatrix}$$

At this point two approaches were made in order to compare their outcome and validate the calculations. First approach is to change the origin of the hexapod to coincide with the location of the tip-point, which can be done by the hexapod controller software. While the second approach is calculating the position of the plate by knowing, or determining the tip-point position by using inverse kinematics.

For the second approach, first step is to find the homogenous transformation matrix, $H_0^{p\prime}$ that describes the needed position of the hexapod plate, in order to achieve the desired tool-tip position. This can be done by post-multiplying the overall homogenous transformation matrix (found from the desired position) with the transpose of H_p^3 such result will yield the homogenous transformation matrix of the plate for the desired tool position.

From the fact that

$$H_0^{3\prime} = H_0^{p\prime} H_p^3$$

We get,

$$H_0^{p\prime} = H_0^{3\prime} H_p^{3\,-1}$$

At this point the translation of the plate with respect to the base reference frame can be easily found as,

$$x = h_{14,}\ y = h_{24,}\ z = h_{34,}$$

While the first three elements of the fourth column in $H_0^{p\prime}$. While for the Euler's angle they can be extracted as follows,

$$\sin\beta = [1 \quad 0 \quad 0 \quad 0\,] H_0^{p\prime} \begin{bmatrix} 0 \\ 0 \\ 1 \\ 0 \end{bmatrix} = h_{13}$$

and,

$$-\sin\alpha\cos\beta = [0 \quad 1 \quad 0 \quad 0\,] H_0^{p\prime} \begin{bmatrix} 0 \\ 0 \\ 1 \\ 0 \end{bmatrix} = h_{23}$$

and,

$$\cos\alpha\cos\beta = [0 \quad 0 \quad 1 \quad 0\,] H_0^{p\prime} \begin{bmatrix} 0 \\ 0 \\ 1 \\ 0 \end{bmatrix} = h_{33}$$

and,

$$-\cos\beta\sin\gamma = [1 \quad 0 \quad 0 \quad 0\,] H_0^{p\prime} \begin{bmatrix} 0 \\ 1 \\ 0 \\ 0 \end{bmatrix} = h_{12}$$

and,

$$\cos\gamma\cos\beta = [1 \quad 0 \quad 0 \quad 0\,]H_0^{p'}\begin{bmatrix}1\\0\\0\\0\end{bmatrix} = h_{11}$$

Therefore,

$$\beta = arcsin\, h_{13}\ or\ \arcsin\pi - h_{13}$$

and,

$$\alpha = \arctan(-\frac{h_{23}}{\cos\beta}, \frac{h_{33}}{\cos\beta})$$

and,

$$\gamma = \arctan(-\frac{h_{12}}{\cos\beta}, \frac{h_{11}}{\cos\beta})$$

It is worth mention that there are two solutions and both give the same result.

Finally, in the equations above, the 6 parameters $(x, y, z, \alpha, \beta, \gamma)$ can be given to the hexapod controller in order to get the desired tool-tip position while compensating the offset error imposed by the parts discussed before. These 6 parameters are entered to the control software (was explained in **Error! Reference source not found.**).

In order to measure the error directly, the cBN wheel's cylindrical geometry can be utilized. For this, a laser displacement sensor is put to the base of the setup. While the Hexapod is moving the spindle, the laser displacement sensor collects a point cloud data of the surface of the cBN tool's root (which is a cylindrical steel). This point cloud data is registered to a cylindrical shape using the SolidWorks' point cloud meshing tools. The results of the construction are shown in **Figure 37** and **Figure 38**. Using the SolidWorks' measurement tools, wheel root radius is calculated. It is observed that the radius is the same with a caliper reading. However, since the laser sensor doesn't account for X and Y motion of the tool, the orientation of the tool miscalculated. But this study opened up a way to incorporate direct calibration of the kinematic errors for future studies. One of the reasons that this study failed was the poor construction of the laser sensor base (from rapid prototyping). To make it work,

the relative orientation error (due to mounting the laser sensor to the base of the robot) of the laser sensor must be calibrated as well.

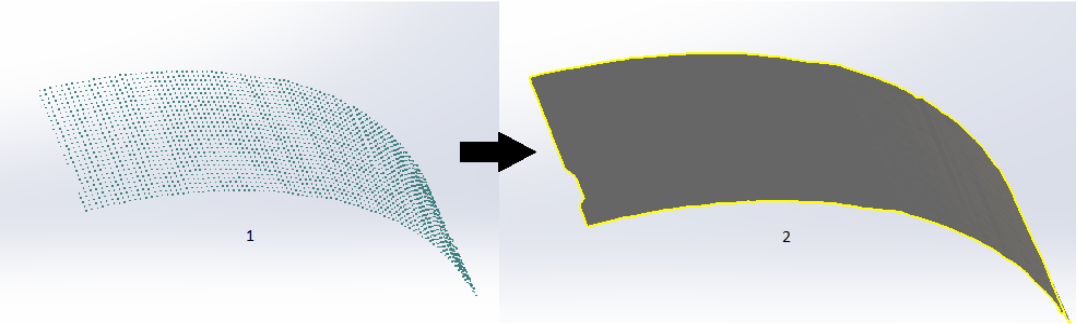

Figure 37 - Surface reconstructon of the cBN wheel root, using the point cloud data and SolidWorks.

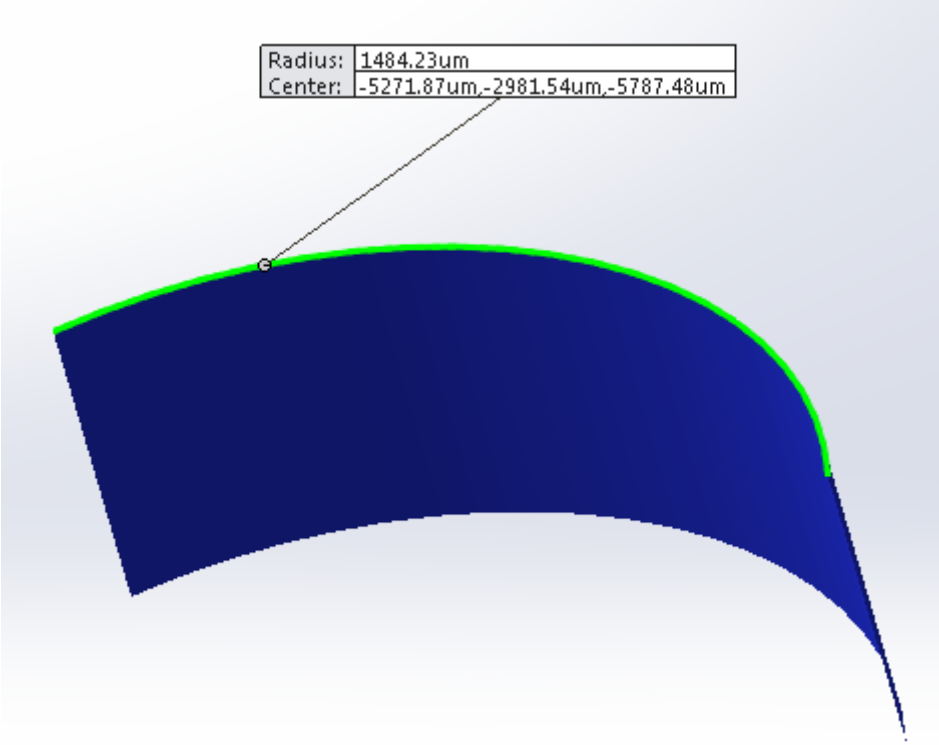

Figure 38 - Radius of the constructed part cylinder. It is same as caliper reading.

CHAPTER 6

CONCLUSION AND FUTURE WORK

6.1. Conclusion

In this study the grinding forces for robotic grinding processes are investigated. The experimental setup and the measured values of the forces and torques showed that a parallel manipulator is suitable for precision robotic grinding operations (that its stiffness and accurate motion allow precision grinding). The experimental data sets are collected via a multi-threaded software and exported for each experiment.

The experimental setup houses the base for the design of a hybrid parallel-serial grinding machine. The serial manipulator can be introduced easily by mounting the experimental setup's relevant parts as an end-effector.

According the Neural Network model given Section 4.4 the peak normal forces are predicted with %10 accuracy. Since the experiments are performed only once, within 80 experiments, something may went wrong. Because of the outliers encountered during the experiments, the model errors changes abruptly in a few cases. These outliers (they are called outliers because the repetition of a few experiments revealed that they have wrong measurements) can be eliminated by repeating high prediction error experiments and fitting a new neural network based on the new experiments.

ANN model is simply a means for testing the experimental setup. Since the setup is a custom-built robotic grinding machine, there had to be a ground model that we can count on. Based on this ground model, more advanced models can be developed. Mapping multiple inputs (spindle speed, depth of cut, and feed-rate) to the outputs (normal and tangential forces) by ANN only produces a black-box relationship.

As observed in the VEC tests, the normal force during the penetration and the tangential grinding cases are the same. Therefore, the penetration tests can be used to predict the normal force also for tangential (lateral) grinding. It should also be mentioned that the normal force is the main control parameter for a force control scenario.

The experiments were done on a well-defined workpiece shape and single workpiece material. This led to the easily recognizable grinding force patterns and made model development straightforward. In the study, the use of cBN tools are justified by showing the tool performance, and ambiguities due to abrasive material (wear, thermal instability, etc.) were in fact had little presence during the studies.

6.2. Future Work

Analysis of the burr removal in deburring process, including the prediction of the cutting forces and the surface quality can be the next phase of this study. Also, the penetration tests defined in this thesis which are easy to perform, can be used to understand the workpiece material properties in a few simple test.

Since the experimental setup has additional capabilities (piezo actuator and the ability to mount laser sensors), these will be used for force/impedance control and surface roughness control.

Optimization of the grinding process with respect to the spindle speed, depth of cut, and number of passes for better surface quality and predictability of the resulting surface, based on the model developed in the thesis is also promising. Thermally stabilizing the environment with a computer controlled thermal compensation and understanding the thermal effects of the grinding parameters also deserve to be mentioned for further research. The Neural Network code mentioned earlier will be finished and combined with physical and empirical modeling approaches.

The knowledge gained while building the experimental setup will be used for developing a hybrid serial-parallel robotic deburring system.

REFERENCES

[1] M. Cronin, "citizen-times," 2014. [Online]. Available: http://www.citizen-times.com/story/news/local/2014/10/14/asheville-home-us-plant-jet-engine-part/17264041/. [Accessed: 20-Aug-2015].

[2] Z. Pandilov and V. Dukovski, "Comparison of the Characteristics Between Serial and Parallel Robots," *Acta Teh. Corviniensis*, 2014.

[3] N. Hogan, "Impedance Control: An Approach to Manipulation," *Am. Control Conf. 1984 IS - SN - VO -*, no. March, pp. 304–313, 1985.

[4] A. Lopes and F. Almeida, "A force–impedance controlled industrial robot using an active robotic auxiliary device," *Robot. Comput. Integr. Manuf.*, vol. 24, no. 3, pp. 299–309, 2008.

[5] I. Marinescu, M. Hitchiner, and E. Uhlmann, *Handbook of machining with grinding wheels*. CRC Press, 2007.

[6] Y. Sun, D. J. Giblin, and K. Kazerounian, "Accurate robotic belt grinding of workpieces with complex geometries using relative calibration techniques," *Robot. Comput. Integr. Manuf.*, vol. 25, no. 1, pp. 204–210, 2009.

[7] M. G. Her and H. Kazerooni, "Automated Robotic Deburring of Parts Using Compliance Control," *J. Dyn. Syst. Meas. Control*, vol. 113, no. MARCH 1991, p. 60, 1991.

[8] K. FUH and S. WANG, "Force Modeling and Forecasting in Creep Feed Grinding Using Improved BP Neural Network," *Int. J. Mach. Tools Manuf.*, vol. 37, no. 8, pp. 1167–1178, 1997.

[9] "Paras Diamond Co.," 2015. [Online]. Available: http://www.ezdressers.com/diamond-cbn-internal-grinding-wheels.htm. [Accessed: 20-Aug-2015].

[10] W. Chen, "Cutting forces and surface finish when machining medium hardness steel using CBN tools," *Int. J. Mach. Tools Manuf.*, vol. 40, no. 3, pp. 455–466, 2000.

[11] X. Chen, W. B. Rowe, and R. Cai, "Precision grinding using CBN wheels," *Int. J. Mach. Tools Manuf.*, vol. 42, no. 5, pp. 585–593, 2002.

[12] W. B. Rowe, *Principles of Modern Grinding Technology*, 1st ed. William Andrew, 2009.

[13] E. Brinksmeier, J. C. Aurich, E. Govekar, C. Heinzel, H.-W. Hoffmeister, F. Klocke, J. Peters, R. Rentsch, D. J. Stephenson, E. Uhlmann, K. Weinert, and M. Wittmann, "Advances in Modeling and Simulation of Grinding Processes," *CIRP Ann. - Manuf. Technol.*, vol. 55, no. 2, pp. 667–696, 2006.

[14] H. K. Tönshoff, J. Peters, I. Inasaki, and T. Paul, "Modeling and Simulation of Grinding Processes," *CIRP Ann.*, vol. 41, no. 2, pp. 677–688, 1992.

[15] X. Li, "Modeling and simulation of grinding processes based on a virtual wheel model and microscopic interaction analysis," WORCESTER POLYTECHNIC INSTITUTE, 2010.

[16] I. Grabec and W. Sachse, *Synergetics of Measurement, Prediction and Control*. Springer-Verlag Berlin Heidelberg, 1997.

[17] M. H. Hassoun, *Fundamentals of Artificial Neural Networks*, 1st ed. Cambridge, MA, USA: MIT Press, 1995.

[18] T. Warren Liao and L. J. Chen, "A neural network approach for grinding processes: Modelling and optimization," *Int. J. Mach. Tools Manuf.*, vol. 34, no. 7, pp. 919–937, Oct. 1994.

[19] B. Csáji, "Approximation with artificial neural networks," *Fac. Sci. Etvs Lornd Univ. Hungary*, 2001.

[20] G. Cybenko, "Degree of approximation by superpositions of a sigmoidal function," *Math. Control. signals Syst.*, vol. 9, no. 3, pp. 303–314, 1989.

[21] K. Hornik, "Approximation capabilities of multilayer feedforward networks," *Neural Networks*, vol. 4, no. 2, pp. 251–257, Jan. 1991.

[22] S. Haykin, *Neural Networks: A Comprehensive Foundation*, 2nd ed. Upper Saddle River, NJ, USA: Prentice Hall PTR, 1998.

[23] L. Fausett, Ed., *Fundamentals of Neural Networks: Architectures, Algorithms, and Applications*. Upper Saddle River, NJ, USA: Prentice-Hall, Inc., 1994.

[24] J.-S. Kwak and M.-K. Ha, "Neural network approach for diagnosis of grinding operation by acoustic emission and power signals," *J. Mater. Process. Technol.*, vol. 147, no. 1, pp. 65–71, Mar. 2004.

[25] Z. Wang, P. Willett, P. R. DeAguiar, and J. Webster, "Neural network detection of grinding burn from acoustic emission," *Int. J. Mach. Tools Manuf.*, vol. 41, no. 2, pp. 283–309, Jan. 2001.

[26] K. S. Narendra and K. Parthasarathy, “Identification and control of dynamical systems using neural networks,” *Neural Networks, IEEE Trans.*, vol. 1, no. 1, pp. 4–27, Mar. 1990.

[27] K. P. Murphy, *Machine Learning: A Probabilistic Perspective*. The MIT Press, 2012.

[28] MATLAB, *version 8.6.0 (R2014a)*. Natick, Massachusetts: The MathWorks Inc., 2014.

[29] L. Liao, F. (Jeff) Xi, and K. Liu, “Modeling and control of automated polishing/deburring process using a dual-purpose compliant toolhead,” *Int. J. Mach. Tools Manuf.*, vol. 48, pp. 1454–1463, 2008.

[30] S. C. Chen and P. C. Tung, “Application of a rule self-regulating fuzzy controller for robotic deburring on unknown contours,” *Fuzzy Sets Syst.*, vol. 110, no. 3, pp. 341–350, 2000.

[31] “ATI Industrial Automation.” [Online]. Available: http://www.ati-ia.com/products/deburr/deburring_home.aspx. [Accessed: 25-Aug-2015].

[32] M. Leonesio, P. Parenti, A. Cassinari, G. Bianchi, and M. Monno, “A Time-Domain Surface Grinding Model for Dynamic Simulation,” *Procedia CIRP*, vol. 4, pp. 166–171, 2012.

[33] B. Zhang, J. Wang, F. Yang, and Z. Zhu, “The effect of machine stiffness on grinding of silicon nitride,” *Int. J. Mach. Tools Manuf.*, vol. 39, no. 8, pp. 1263–1283, 1999.

[34] A. A. Akbari and S. Higuchi, “Autonomous tool adjustment in robotic grinding,” *J. Mater. Process. Technol.*, vol. 127, no. 2, pp. 274–279, 2002.

[35] D. Zhu, S. Luo, L. Yang, W. Chen, S. Yan, and H. Ding, “On energetic assessment of cutting mechanisms in robot-assisted belt grinding of titanium alloys,” *Tribol. Int.*, vol. 90, pp. 55–59, 2015.

[36] “lubbulletin.” [Online]. Available: http://www.labbulletin.com/articles/PI-Hexapods-chosen-for-space-mission#.VhY_kvmqqko. [Accessed: 25-Aug-2015].

[37] “PI H-824.” [Online]. Available: http://www.physikinstrumente.com/product-detail-page/h-824-700815.html. [Accessed: 25-Aug-2015].

[38] “Qt Framework,” 2015. [Online]. Available: http://doc.qt.io/. [Accessed: 20-Aug-2015].

[39] “PFERD,” 2015. [Online]. Available: http://www.pferd.com/images/katalog-205-wzh22-150dpi-tr.pdf. [Accessed: 20-Aug-2015].

[40] I. Kaastra and M. Boyd, “Designing a neural network for forecasting financial and economic time series,” *Neurocomputing*, vol. 10, no. 3, pp. 215–236, Apr. 1996.

[41] F. H. F. Leung, H. K. Lam, S. H. Ling, and P. K. S. Tam, “Tuning of the structure and parameters of a neural network using an improved genetic algorithm,” *Neural Networks, IEEE Trans.*, vol. 14, no. 1, pp. 79–88, Jan. 2003.

APPENDIX A

SPECIFICATIONS

A.1. Hexapod Specifications

Table 5 - PI Company Hexapod parallel manipulator specifications.

H-824.Gxx			
Active axes	*$X, Y, Z, \theta_x, \theta_y, \theta_z$*	*Max. Velocity $\theta_x, \theta_y, \theta_z$*	*11 mrad/s*
Motion and positioning		*Typ. Velocities for X, Y, Z*	*0.5 mm/s*
Travel Range X, Y	*±22.5 mm*	*Typ. Velocities for $\theta_x, \theta_y, \theta_z$*	*5.5 mrad/s*
Travel Range Z	*±12.5 mm*	*Mechanical Properties*	
Travel Range θ_x, θ_y	*±7.5 °*	*Stiffness X, Y*	*1.7 N/µm*
Travel Range θ_z	*±12.5 °*	*Stiffness Z*	*7 N/µm*
Single actuator design resolution	*0.007 µm*	*Load (base plate horizontal / any orientation)*	*10/5 kg (max)*
Min. incremental motion X, Y, Z	*0.3 µm*	*Holding force, de-energized (base plate horizontal / any orientation)*	*100 / 50 N (max)*
Min. incremental motion $\theta_x, \theta_y, \theta_z$	*3.5 µrad*	*Motor type*	*DC gear motor*
Backlash X, Y	*3 µm*	*Miscellaneous*	
Backlash Z	*1 µm*	*Operating temperature range*	*-10 to 50 °C*
Backlash θ_x, θ_y	*20 µrad*	*Material*	*Aluminum*

A.2. Piezo Actuator Specifications

Table 6 - PI Company piezo actuator specifications.

P-602.8S0			
Active axes	*X*	*Drive Properties*	
Motion and positioning		*Piezoceramics*	*PICMA® P-888*
Integrated sensor	*SGS*	*Electrical capacitance*	*39 µF*
Open-loop travel - 20 to 120 V	*1000 µm*	*Dynamic operating current coefficient*	*4 µA/(Hz x µm)*
Closed-loop travel	*1000 µm*	*Miscellaneous*	
Open-loop resolution	*0.5 nm*	*Operating temperature range*	*-10 to 50 °C*
Closed-loop resolution	*7 nm*	*Material*	*Stainless steel*
Closed-loop non-linearity	*1.5 %*	*Dimensions*	*126 mm x 34 mm x 14 mm*
Repeatability	*50 nm*	*Cable length*	*0.5 / 0.5 / 2 m*
Mechanical properties		*Miscellaneous*	
Stiffness in motion direction	*0.4 N/µm*		
Unloaded resonant frequency	*150 Hz*		

A.3. Multi-Axis Force/Torque Sensor Specifications

Table 7 - Multi-axis force/torque sensor specifications (ATI Gamma IP60).

$F_{x/y}$	*±1200 N*
F_z	*±4100 N*
$T_{x/y}$	*±79 Nm*
T_z	*±82 Nm*
X-axis & Y-axis forces (K_x, K_y)	*9.1x10^{6}N/m*
Z-axis force (K_z)	*1.8x10^{7}N/m*
X-axis & Y-axis torque (K_{tx}, K_{ty})	*1.1x10^{4}Nm/rad*
Z-axis torque (K_{tz})	*1.6x10^4 Nm/rad*
F_x, F_y, T_z	*1400 Hz*
F_z, T_x, T_y	*2000 Hz*
Weight	*0.255 kg*
Diameter	*75.4 mm*
Height	*33.3 mm*

A.4. Spindle Specifications

221-42-MHP

High-frequency spindle
Pneumatic direct tool change

Spindle for high-speed milling, -grinding, -drilling, -engraving

Technical specifications

- High precision hybrid ball bearings – 2 Pcs.
- Lifetime lubricated, maintenance free
- Motor: type 2
- Nominal output power: max. 0,3 kW
- Voltage: max.43 V
- Current: max. 7 A
- Frequency: max. 1000Hz
- Motor poles: 1 pair
- Rotation speed: max. 60.000 rpm
- Motor protection: thermistor
- Speed monitoring: transmitter
- Sealing-air
- Housing diameter: 42 mm
- Cooling system: non cooled
- Tool change: pneumatic direct tool change
- Clamping range: up to 6 mm (1/4")
- Coupler plug: 7-pole plastics
- Weight: 2,2 kg

Dimensions

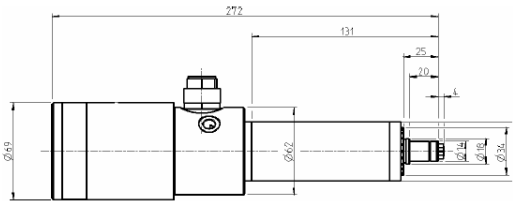

Power-, torque- and speed diagram

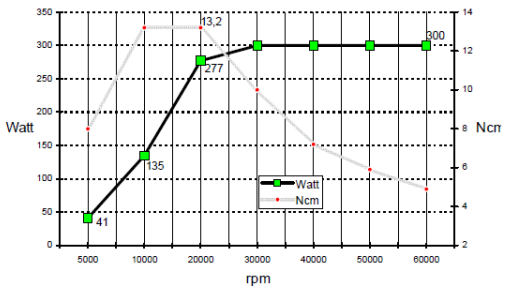

BMR GmbH • elektrischer & elektronischer Gerätebau
Unterreichenbacher Straße 1• D-90455 Nürnberg-Katzwang
Tel. +49 (0)9122-631480 • Fax + 49 (0)9122-6314829
info@bmr-gmbh.de www.bmr-gmbh.de

Figure 39 - BMR spindle specifications.

APPENDIX B

TECHNICAL DRAWINGS

B.1. Tool Holder

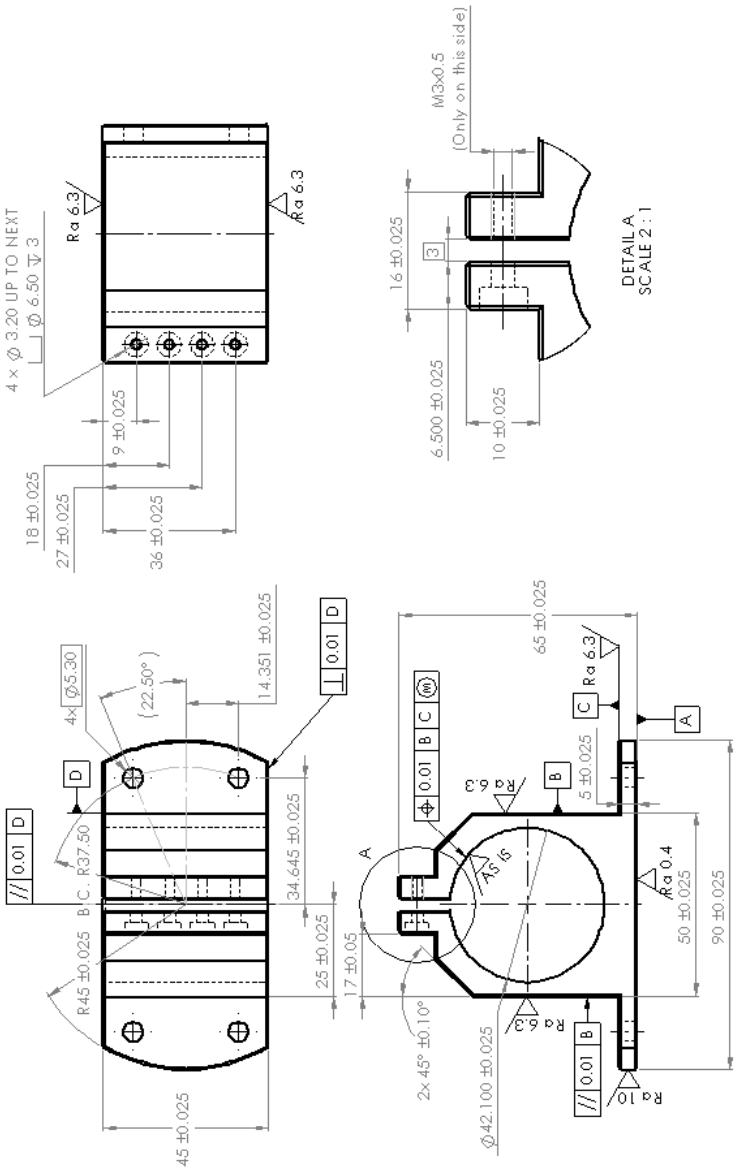

Figure 40 - Tool holder. Material Al7060

B.2. Hexapod to System 3-R Connection Plate

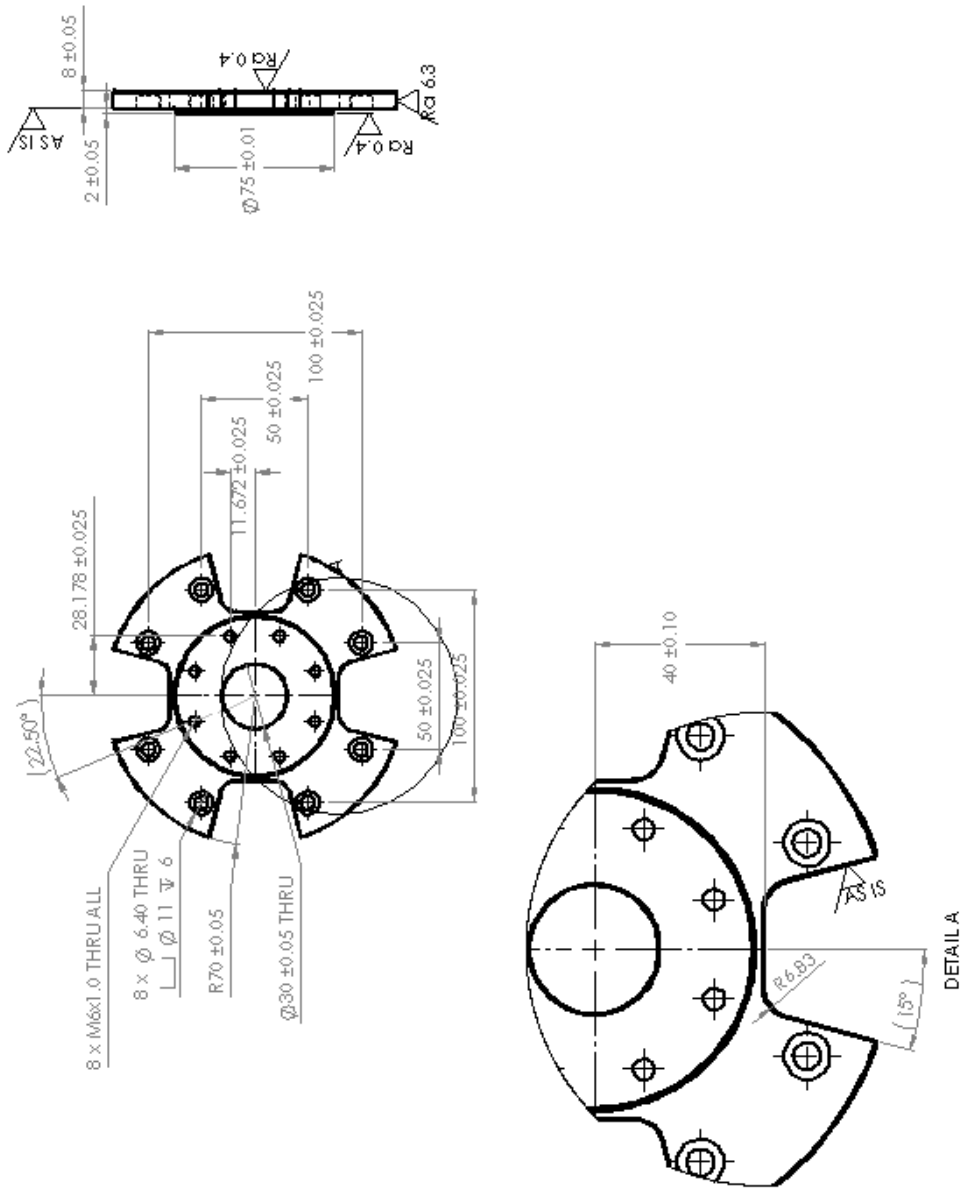

Figure 41 - Hexapod to System 3-R tool changer connection plate. Material Al7060

B.3. Force/Torque Sensor to Tool Holder Connection Plate

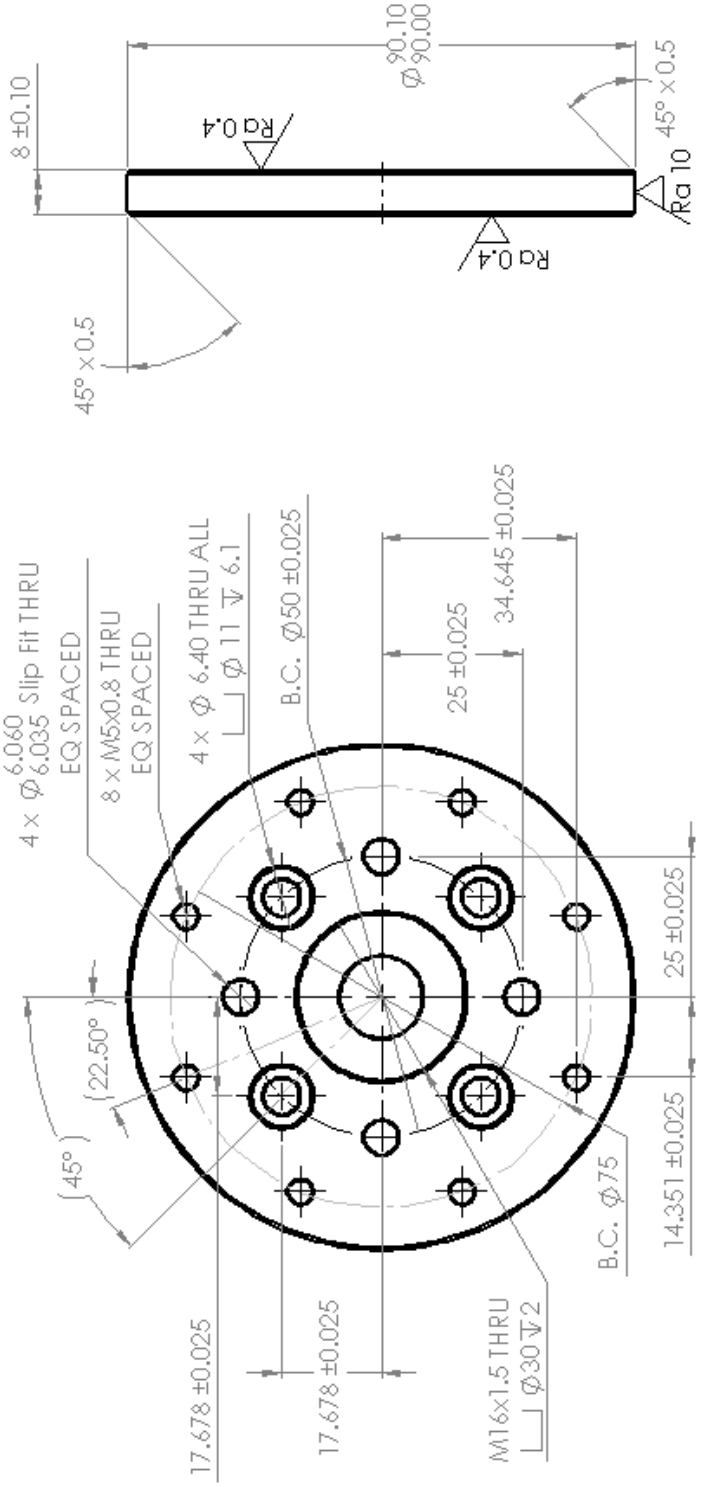

Figure 42 - Force/Torque sensor to tool holder connection plate. Material Al7060

B.4. System 3-R to Force/Torque Sensor Connection Plate

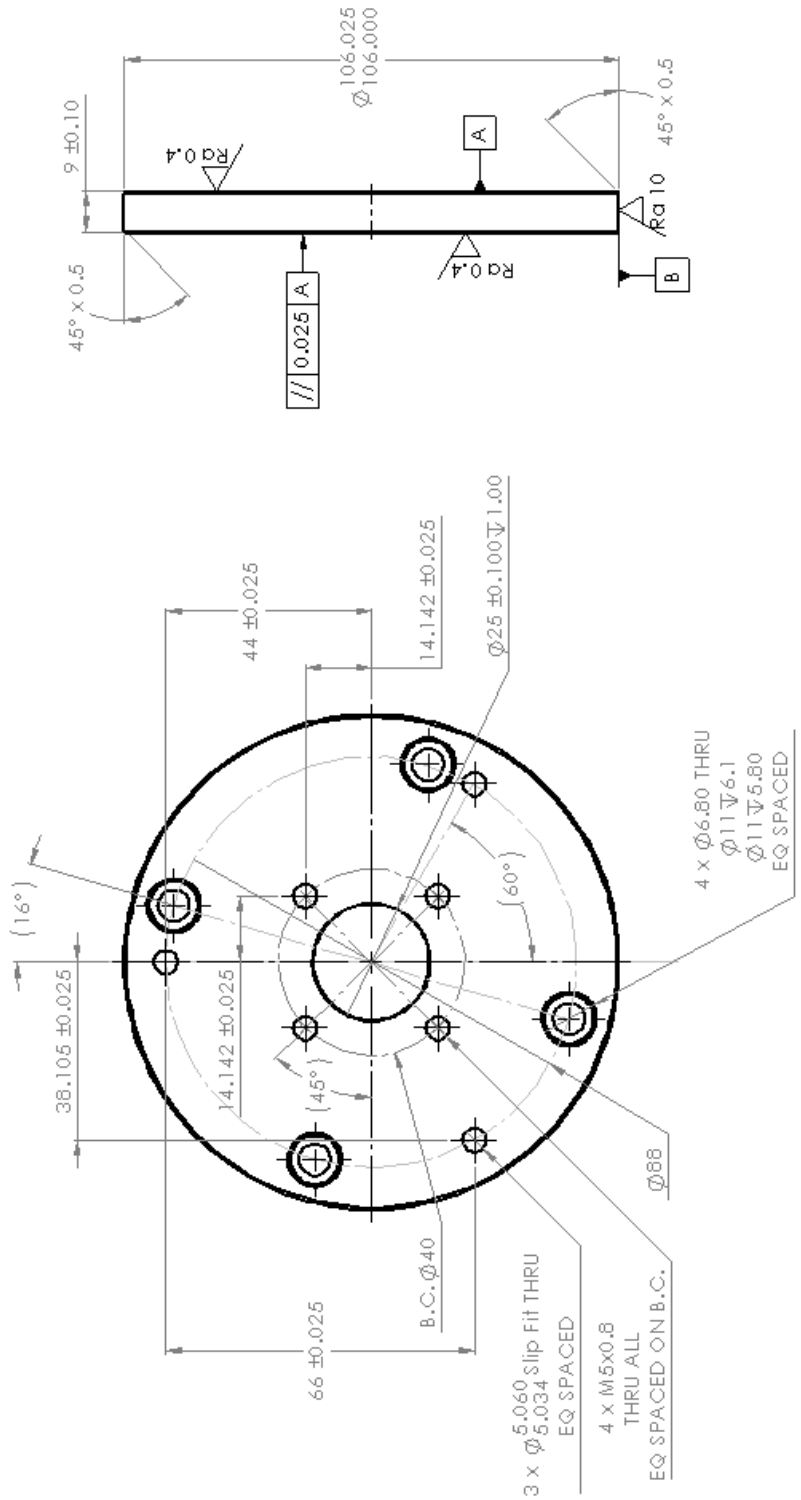

Figure 43 - System 3-R to Force/Torque sensor connection plate. Material Al7060

B.5. Side Plates

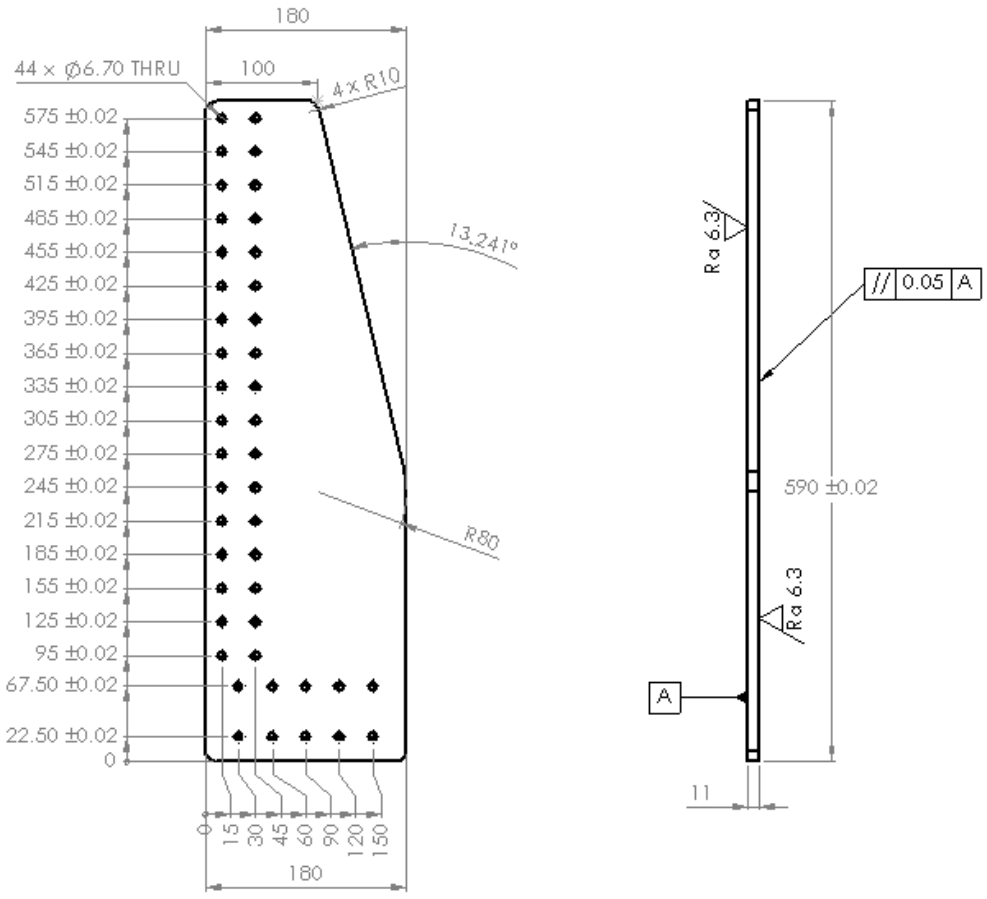

Figure 44 - Technical drawing of the side plates (2 identical plates are manufactured).Material St37.

B.6. Back Plate

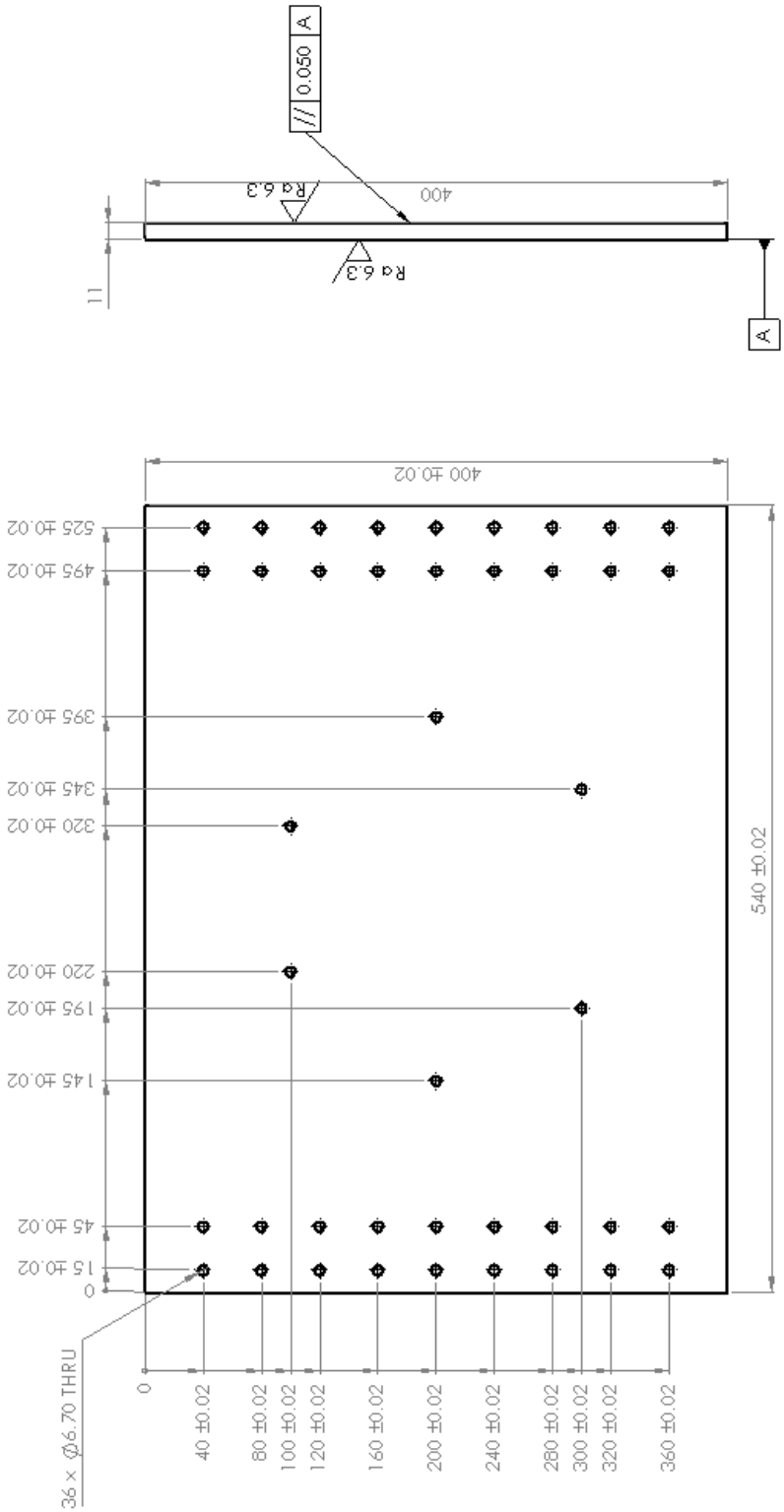

Figure 45 - Technical drawing of the back plate. Material St37.

B.7. X Axis to Y Axis Connection Plate

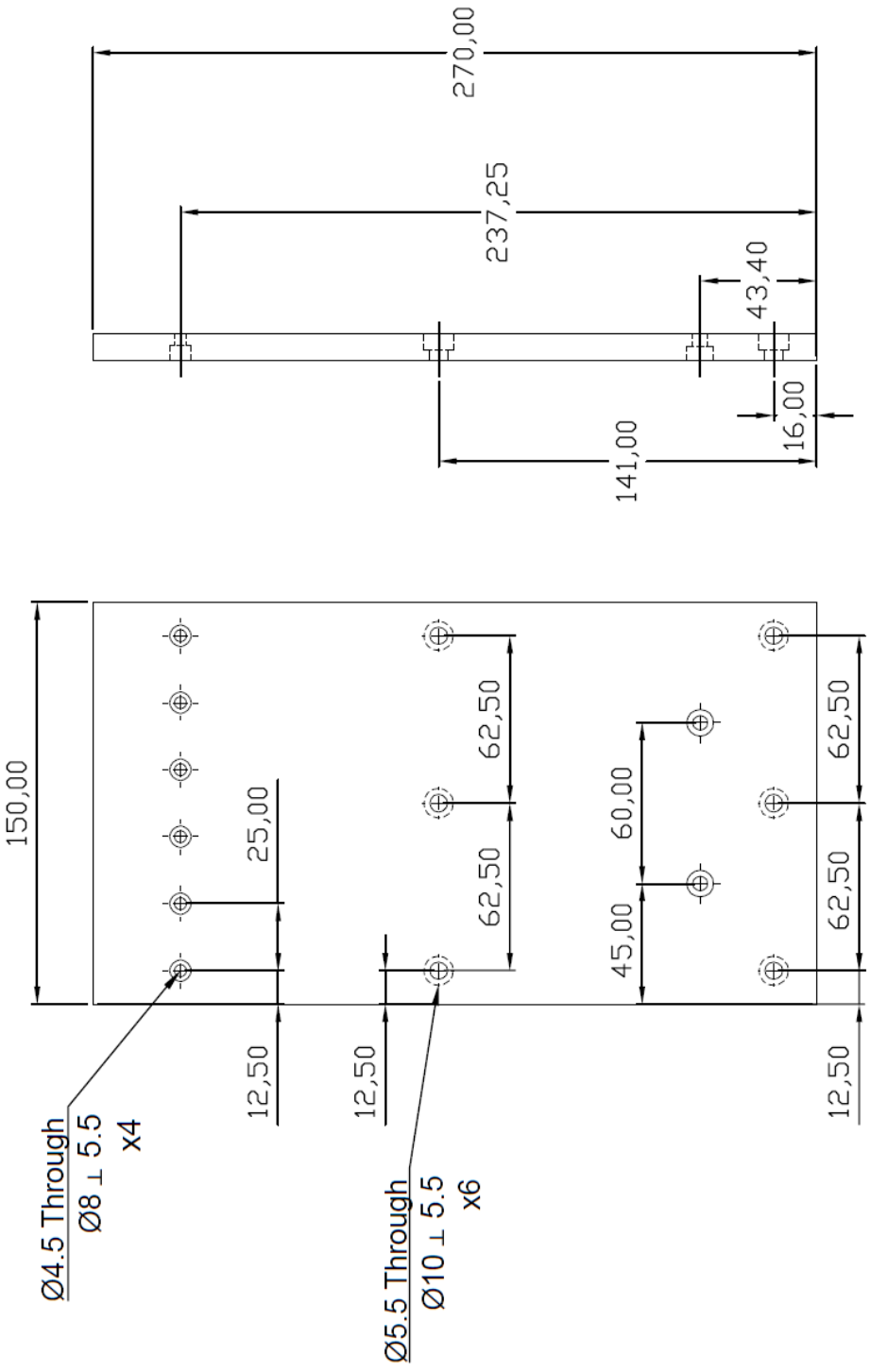

Figure 46 - X axis to Y axis connection plate for lower linear stages. Material Al7060.

B.8. Piezo Table to Sample Holder Connection Plate

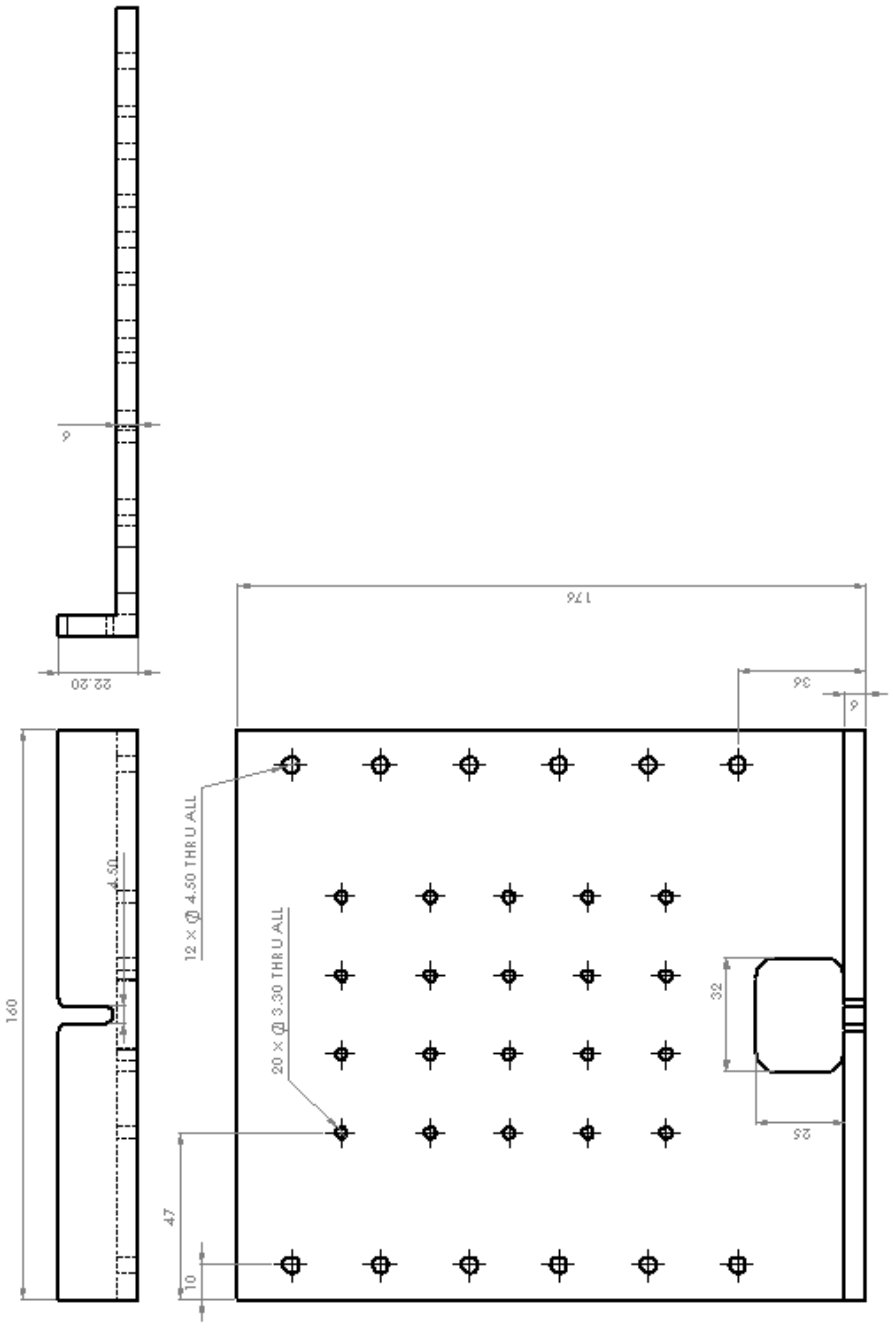

Figure 47 - Piezo actuator to sample holder and y axis connection plate. Material Al7060.

B.9. Sample Holder

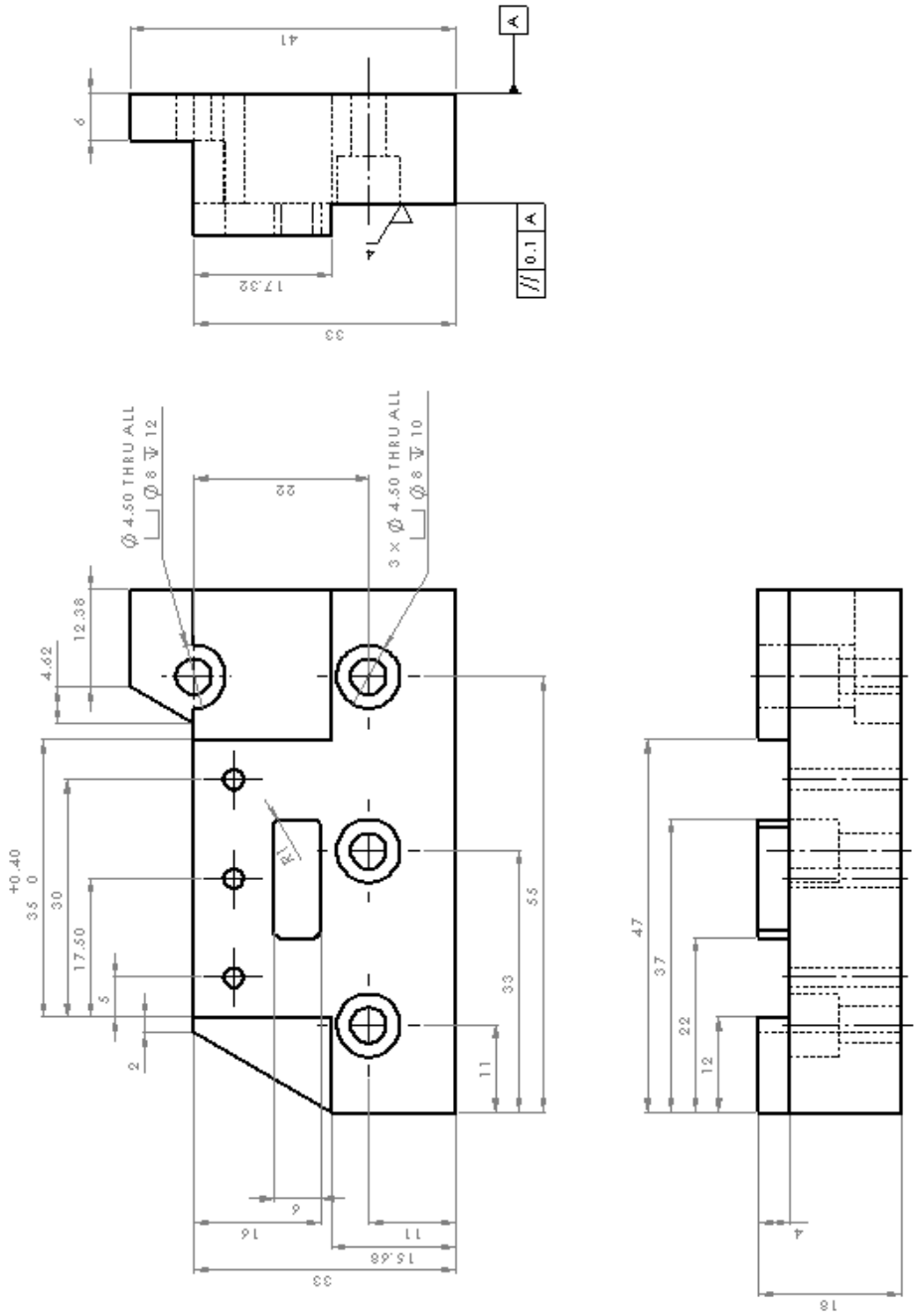

Figure 48 - Technical drawing of the sample holder. Material Al7060.

B.10. Piezo Actuator Constraining Plate

Piezo actuator is connected to this part and the part given in Appendix B.8. These two plates restricts the piezo actuator and that makes the actuator move the samples that are connected to the fixture given in Appendix B.9.

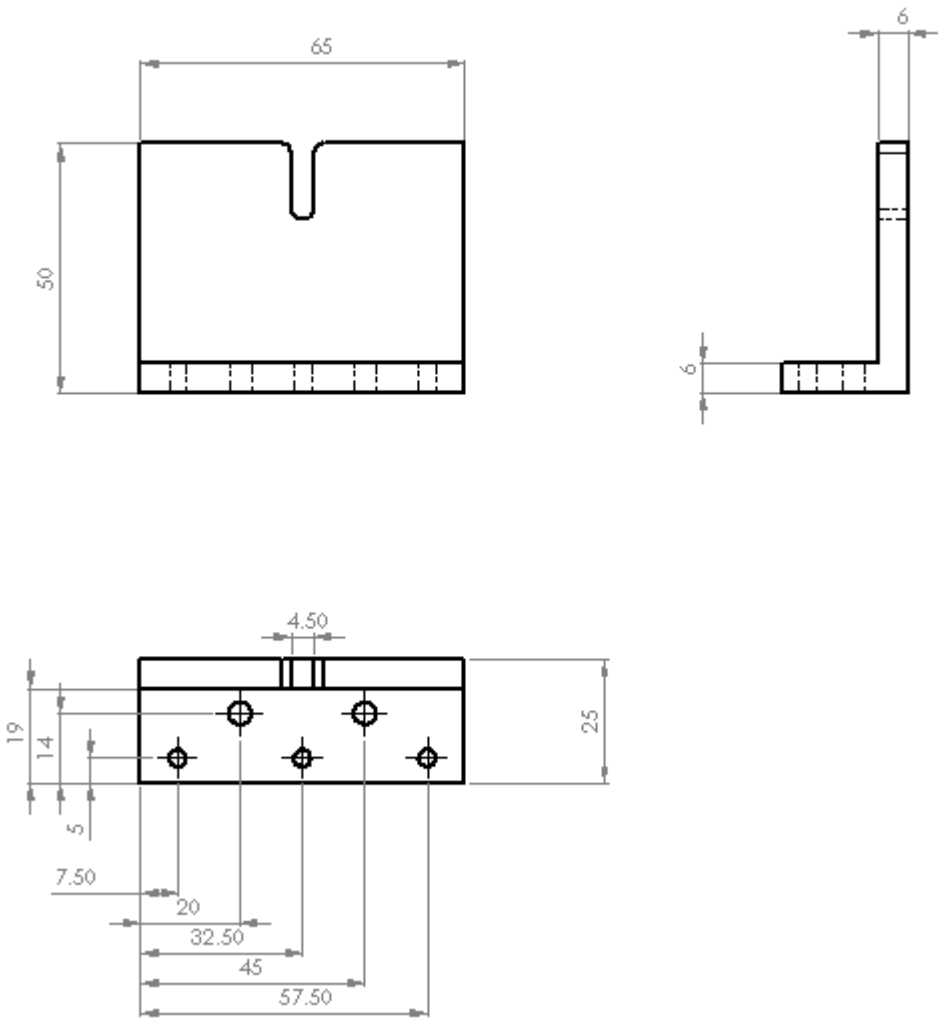

Figure 49 - Technical drawing of the piezo actuator constraining plate.

This part is manufactured from Al7060 and the tolerances are not given on the drawing because of the fact that it has adjustment groove (±0.1 mm tolerances).

APPENDIX C

SCRIPTS AND PENETRATION EXPERIMENT RESULTS

C.1. Filtering Code

Since the data coming from the F/T sensor is originally possess measurement noise, the parameters of the model cannot be found without a proper filtering method.

The filtering is achieved by the following function, which calculates moving averages of the data with a given window size. This code also converts the unit of the torque values.

FaU.m

```
% FaU is short for filtering and unit conversion.
function [Fx,Fy,Fz,Tx,Ty,Tz] = FaU(v1,v2,v3,v4,v5,v6, level)
B = (1/level)*ones(level,1); % Moving average filter.
Fx = filter(B, 1, v1); % Filter Fx component.
Fy = filter(B, 1, v2); % Filter Fy component.
Fz = filter(B, 1, v3); % Filter Fz component.
Tx = filter(B, 1, v4); Tx = 100*Tx; % Filter Tx and convert unit from Nm->Nmm
Ty = filter(B, 1, v5); Ty = 100*Ty; % Filter Ty and convert unit from Nm->Nmm
Tz = filter(B, 1, v6); Tz = 100*Tz; % Filter Tz and convert unit from Nm->Nmm
End
```

C.2. Kinematic Offset Error Calculation MATLAB Code

The kinematic offset calculation necessary to move the Hexapod to the corrected position is provided in this section as follows,

kinematic_offset.m

```
clc
clear all
syms alpha beta gama X0 Y0 Z0 L1 L2 psi zeta P1 delta_alpha delta_beta
delta_gama delta_X delta_Y delta_Z
C0P=[1 0 0;0 cos(alpha) -sin(alpha);0 sin(alpha) cos(alpha)]*[cos(beta) 0
sin(beta);0 1 0;-sin(beta) 0 cos(beta)]*[cos(gama) -sin(gama) 0;sin(gama)
cos(gama) 0;0 0 1];
CP1=[1 0 0 ;0 1 0 ;0 0 1];
C12=[cos(psi) -sin(psi) 0;sin(psi) cos(psi) 0;0 0 1];
C23=[cos(zeta) 0 sin(zeta);0 1 0;-sin(zeta) 0 cos(zeta)];
C03=C0P*CP1*C12*C23;
C03_prime=C03*[1 0 0;0 cos(delta_alpha) -sin(delta_alpha);0 sin(delta_alpha)
cos(delta_alpha)]*[cos(delta_beta) 0 sin(delta_beta);0 1 0;-sin(delta_beta) 0
cos(delta_beta)]*[cos(delta_gama) -sin(delta_gama) 0;sin(delta_gama)
cos(delta_gama) 0;0 0 1];
T0P=[cos(beta)*cos(gama) -cos(beta)*sin(gama) sin(beta)
X0;sin(alpha)*sin(beta)*cos(gama)+cos(alpha)*sin(gama) -
sin(alpha)*sin(beta)*sin(gama)+cos(alpha)*cos(gama) -sin(alpha)*cos(beta) Y0;-
cos(alpha)*sin(beta)*cos(gama)+sin(alpha)*sin(gama)
cos(alpha)*sin(beta)*sin(gama)+sin(alpha)*cos(gama) cos(alpha)*cos(beta) Z0;0 0
0 1];
TP1=[1 0 0 0;0 1 0 0;0 0 1 L1;0 0 0 1];
T12=[cos(psi) -sin(psi) 0 0;sin(psi) cos(psi) 0 0;0 0 1 L2;0 0 0 1];
T23=[cos(zeta) 0 sin(zeta) -P1;0 1 0 0;-sin(zeta) 0 cos(zeta) 0;0 0 0 1];
T03=T0P*TP1*T12*T23;
syms dum
T03_prime=[dum dum dum dum;dum dum dum dum;dum dum dum dum;dum dum
dum dum];
T03_prime(1,1)=C03_prime(1,1);
T03_prime(1,2)=C03_prime(1,2);
T03_prime(1,3)=C03_prime(1,3);
T03_prime(2,1)=C03_prime(2,1);
T03_prime(2,2)=C03_prime(2,2);
```

```
T03_prime(2,3)=C03_prime(2,3);
T03_prime(3,1)=C03_prime(3,1);
T03_prime(3,2)=C03_prime(3,2);
T03_prime(3,3)=C03_prime(3,3);
T03_prime(1,4)=T03(1,4)+delta_X;
T03_prime(2,4)=T03(2,4)+delta_Y;
T03_prime(3,4)=T03(3,4)+delta_Z;
T03_prime(4,4)=1;
T0P_prime=T03_prime*inv(T23)*inv(T12)*inv(TP1);
X_prime=T0P_prime(1,4);
Y_prime=T0P_prime(2,4);
Z_prime=T0P_prime(3,4);
h13=T0P_prime(1,3);
h23=T0P_prime(2,3);
h33=T0P_prime(3,3);
h12=T0P_prime(1,2);
h11=T0P_prime(1,1);
beta_prime1=atan2(h13,(sqrt(1-(h13^2))));
beta_prime2=atan2(h13,(-sqrt(1-(h13^2))));
alpha_prime1=atan2((-h23/cos(beta_prime1)),(h33/cos(beta_prime1)));
alpha_prime2=atan2((-h23/cos(beta_prime2)),(h33/cos(beta_prime2)));
gama_prime1=atan2((-h12/cos(beta_prime1)),(h11/cos(beta_prime1)));
gama_prime2=atan2((-h12/cos(beta_prime2)),(h11/cos(beta_prime2)));
```

C.3. Penetration Experiment Results

The 80 penetration experiment force measurements are collected in this appendix. These are the net forces when the cable forces (cables of the spindle and the force/torque sensor introduce errors) are subtracted.

Table 8 - Penetration experiment results (80 experiments). N means peak normal force, and T means peak tangential force. It also shows the experiment number in parenthesis.

(1) *N: 2.41* *T: 1.98*	*(5)* *N: 9.27* *T: 9.91*	*(9)* *N: 17.22* *T: 17.48*	*(13)* *N: 24.97* *T: 22.38*
(2) *N: 4.21* *T: 4.87*	*(6)* *N: 12.02* *T: 13.35*	*(10)* *N: 20.15* *T: 22.12*	*(14)* *N: 30.25* *T: 28.06*
(3) *N: 4.72* *T: 5.46*	*(7)* *N: 12.73* *T: 14.59*	*(11)* *N: 21.6* *T: 24.66*	*(15)* *N: 32.53.* *T: 30.74*
(4) *N: 4.84* *T: 4.844*	*(8)* *N: 13.15* *T: 15.11*	*(12)* *N: 22.26* *T: 25.4*	*(16)* *N: 34.4* *T: 31.95*
(17) *N: 4.90* *T: 4.58*	*(21)* *N: 11.59* *T: 10.57*	*(25)* *N: 17.81* *T: 15.57*	*(29)* *N: 24.54* *T: 20.80*
(18) *N: 5.42* *T: 5.15*	*(22)* *N: 13.82* *T: 13.41*	*(26)* *N: 21.27* *T: 20.21*	*(30)* *N: 28.91* *T: 26.44*
(19) *N: 6.17* *T: 5.83*	*(23)* *N: 13.91* *T: 13.01*	*(27)* *N: 22.21* *T: 22.53*	*(31)* *N: 30.89* *T: 28.73*

Table 8 - Penetration experiment results (80 experiments). N means peak normal force, and T means peak tangential force. It also shows the experiment number in parenthesis. (continued)

(20) *N: 6.27* *T: 5.826*	*(24)* *N: 14.19* *T: 14.04*	*(28)* *N: 23.42* *T: 23.46*	*(32)* *N: 31.92* *T: 33.41*
(33) *N: 4.93* *T: 4.66*	*(37)* *N: 10.22* *T: 9.54*	*(41)* *N: 16.46* *T: 14.63*	*(45)* *N: 23.01* *T: 19.22*
(34) *N: 5.51* *T: 5.45*	*(38)* *N: 12.17* *T: 12.07*	*(42)* *N: 19.81* *T: 19.64*	*(46)* *N: 27.29* *T: 26.00*
(35) *N: 5.66* *T: 5.53*	*(39)* *N: 13.42* *T: 13.47*	*(43)* *N: 21.42* *T: 21.95*	*(47)* *N: 29.24* *T: 29.00*
(36) *N: 5.52* *T: 5.45*	*(40)* *N: 13.56* *T: 13.57*	*(44)* *N: 21.46* *T: 22.95*	*(48)* *N: 26.35* *T: 27.78*
(49) *N: 5.00* *T: 4.19*	*(53)* *N: 10.25* *T: 8.54*	*(57)* *N: 16.98* *T: 12.57*	*(61)* *N: 23.33* *T: 16.54*
(50) *N: 5.33* *T: 4.71*	*(54)* *N: 12.20* *T: 10.54*	*(58)* *N: 19.52* *T: 17.04*	*(62)* *N: 26.69* *T: 22.02*
(51) *N: 5.96* *T: 5.14*	*(55)* *N: 12.82* *T: 11.78*	*(59)* *N: 20.79* *T: 19.22*	*(63)* *N: 28.69* *T: 25.87*
(52) *N: 4.20* *T: 4.31*	*(56)* *N: 10.52* *T: 10.68*	*(60)* *N: 16.77* *T: 17.44*	*(64)* *N: 21.87* *T: 23.87*

Table 8 - Penetration experiment results (80 experiments). N means peak normal force, and T means peak tangential force. It also shows the experiment number in parenthesis. (continued)

(65) *N: 3.28* *T: 3.53*	*(69)* *N: 6.40* *T: 6.69*	*(73)* *N: 10.25* *T: 9.89*	*(77)* *N: 15.10* *T: 14.40*
(66) *N: 3.72* *T: 4.15*	*(70)* *N: 8.61* *T: 8.98*	*(74)* *N: 13.61* *T: 13.922*	*(78)* *N: 20.35* *T: 21.84*
(67) *N: 3.91* *T: 4.38*	*(71)* *N: 9.25* *T: 10.06*	*(75)* *N: 15.20* *T: 16.79*	*(79)* *N: 22.50* *T: 25.13*
(68) *N: 3.93* *T: 4.16*	*(72)* *N: 10.12* *T: 11.00*	*(76)* *N: 14.03* *T: 17.58*	*(80)* *N: 24.31* *T: 26.85*

APPENDIX D

ELECTRONIC CONNECTIONS

D.1. Piezo Actuator Connections

The piezo actuator was included in the setup design but it was not used during the present work. The actuator is accompanied with its driver. The driver is connected to the piezo actuator by the following electronic connection diagram,

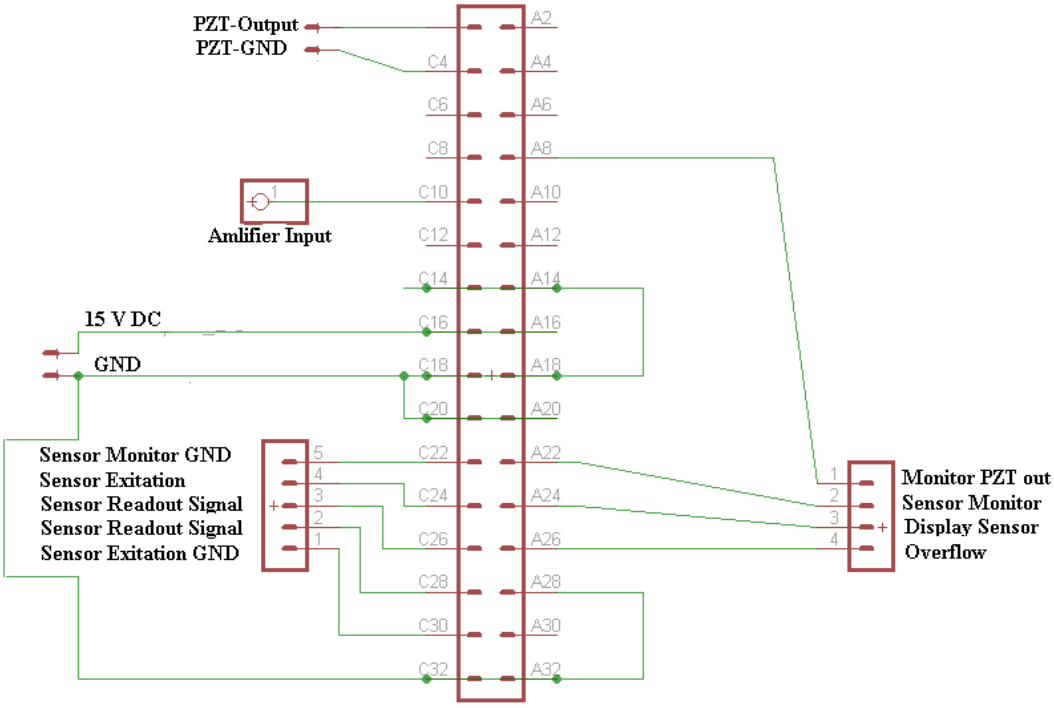

Figure 50 - Connection schema of the PI E-610.S0 LVPZT motion amplifier/controller.